Article

3D nanolithography with metalens arrays and spatially adaptive illumination

https://doi.org/10.1038/s41586-025-09842-x

Received: 20 March 2025

Accepted: 31 October 2025

Published online: 17 December 2025

Check for updates

Songyun Gu[1,7], Chenkai Mao[2,7], Anna Guell Izard[1], Sarvesh Sadana[1], Dongping Terrel-Perez[3], Magi Mettry-Yassa[4], Wonjin Choi[4], Wenjie Zhou[5], Hujie Yan[5], Ziran Zhou[5], Travis Massey[1], Alex Abelson[1], You Zhou[2,6], Sijia Huang[1], Chiara Daraio[5], Thejaswi Umanath Tumkur[4], Jonathan A. Fan[2]✉ & Xiaoxing Xia[1]✉

The growing demand for advanced materials, miniaturized devices and integrated microsystems calls for the reliable fabrication of complex, multiscale, three-dimensional (3D) architectures, a need increasingly addressed through light-based and laser-based processes. However, owing to the field-of-view (FOV) limitations of conventional imaging optics, existing 3D laser nanofabrication techniques face fundamental challenges in throughput, proximity error and stitching defects on the path to scaling. Here we present a scalable 3D nanofabrication platform that uses a metalens-generated focal spot array to parallelize two-photon lithography (TPL)[1] beyond centimetre-scale write field areas. Metalenses are ideally suited for producing submicron-scale focal spots for high-throughput nanolithography, as they uniquely feature large numerical apertures (NAs), immersion media compatibility and large-scale manufacturability. We experimentally demonstrate a printing system that uses a 12-cm^2 metalens array to produce more than 120,000 cooperative focal spots, corresponding to a throughput exceeding 10^8 voxels s^{-1}. By programmatically patterning the focal spot array using a spatial light modulator (SLM), an adaptive parallel printing strategy is developed for precise greyscale linewidth modulation and choreographed printing of semiperiodic and fully aperiodic 3D geometries. We demonstrate parallel printing of replicated microstructures (>50 M microparticles per day), centimetre-scale 3D architectures with feature sizes down to 113 nm, and photonic and mechanical metamaterials. This work demonstrates the potential of 3D nanolithography towards wafer-scale production, showing how TPL could be used at scale for applications in microelectronics[2], biomedicine[3], quantum technology[4] and high-energy laser targets[5,6].

High-volume, rapid fabrication of 3D nanoarchitected materials and devices is key to deploying next-generation nanotechnologies to solve real-world challenges. To address this need, substantial efforts over the past two decades have been made to evolve light-based nanolithography methods from two-dimensional (2D) patterning to true 3D nanostructure formation. The development has been largely driven by TPL, which leverages nonlinear two-photon absorption to perform nanoscale 3D fabrication[1]. TPL uses the scanning of an ultrahigh-intensity femtosecond focal spot inside a photoresin to locally activate photosensitive molecules, leading to controlled polymerization along the scanning trajectory with feature sizes near the optical diffraction limit. Compared with other high-precision additive manufacturing (AM) methods[7–10], TPL uniquely offers sub-micrometre resolution at a robust fabrication throughput (>1 mm^3 h^{-1}). It has served as the basis for a wide range of exciting proof-of-concept lab-scale applications in the domains of microelectronics[2], architected materials[11,12], energy[6], biomedicine[3], and quantum[4] and information technologies[13].

To improve the throughput of TPL, recent efforts have sought to parallelize the process by incorporating optical techniques such as light-sheet projection[14,15] and multibeam scanning[16–21]. Despite substantial advancements, it remains a grand challenge to decouple the trade-off between resolution and speed. Nearly all concepts use conventional imaging objective lenses and operate within their FOVs that are fundamentally limited to hundreds of micrometres, setting bounds to the total write volume without error-prone stitching. Also, the number of focal spots that can be simultaneously illuminated to perform parallel writing within the FOV is constrained by proximity effect[22]: when the focal spots are too close (generally <10 µm), local reaction–diffusion kinetics from photopolymerization occurring at each spot start to interact with one another, causing unwanted overcuring and reduced resolution (discussed in the Supplementary Information).

[1]Materials Engineering Division, Lawrence Livermore National Laboratory, Livermore, CA, USA. [2]Department of Electrical Engineering, Stanford University, Stanford, CA, USA. [3]Computational Engineering Division, Lawrence Livermore National Laboratory, Livermore, CA, USA. [4]Materials Science Division, Lawrence Livermore National Laboratory, Livermore, CA, USA. [5]Division of Engineering and Applied Science, California Institute of Technology, Pasadena, CA, USA. [6]Department of Physics and Optical Science, University of North Carolina at Charlotte, Charlotte, NC, USA. [7]These authors contributed equally: Songyun Gu, Chenkai Mao. ✉e-mail: jonfan@stanford.edu; xia7@llnl.gov

Furthermore, parallel TPL techniques that use fixed diffractive optics to generate focal spot arrays have been shown to enhance fabrication throughput, but they are limited to the printing of specific structures[19,23]. Holographic multifocus scanning can generate 3D focal spot patterns with high flexibility but the generation and use of holograms can lead to practical computing and data transfer bottlenecks[17,18].

In this work, we propose a parallel 3D nanolithography method based on meta-optics arrays. This concept circumvents the throughput bottleneck by eliminating the use of conventional microscopy optics and their associated FOV limitations; it instead uses a large array of high-NA, non-imaging metalenses to expand the number and spatial distribution of focal spots, allowing TPL to be carried out simultaneously at each focal spot (Fig. 1a,b). Crucial to our system is the incorporation of an SLM to shape the intensity of a femtosecond laser beam into arbitrary greyscale patterns (Fig. 1c), enabling a straightforward route to the precise and independent modulation over each focal spot. In the proposed set-up, printing is performed by sandwiching the photosensitive resin between the metalens array and the build substrate and then mechanically scanning the substrate using a three-axis motion stage over microscale distances to form 3D structures. The lateral travel distances within each layer-by-layer print are generally less than the size of a metalens. In this manner, large-scale structures spanning the entire metalens array dimension can be printed with minimal stitching defects thanks to the short lateral travelling distances and the elimination of shadowing effects. We demonstrate TPL printing with an array of more than 120,000 tunable focal spots, which polymerizes the photoresin simultaneously across a 2-inch aperture with a throughput of 1.2×10^8 voxels s^{-1} and a minimum feature size of 113 nm. This strategy is directly scalable with the use of larger metalens arrays, advanced SLMs and more powerful femtosecond lasers, all of which are commercially available. Our parallelization method can be further translated to other laser-based fabrication processes, such as maskless laser lithography[24], glass and metal processing[25], and nanocrystal-assembly-based multimaterial 3D fabrication[26].

Metalens-based TPL

Metasurfaces consist of ensembles of subwavelength phase-shifting elements that collectively serve as optical phase arrays, and they can feature wavefront shaping and polarization responses that exceed the capabilities of bulk optics and scalar diffractive devices[27–29]. Metalenses are uniquely suited to serve as non-imaging focusing elements in our TPL system for several reasons. Metalenses working at near-infrared wavelengths can be made from high-contrast, low-loss dielectric materials such as silicon, which can be designed for durable operation under high-power laser irradiations[30] and used in resin immersion environments. Metalenses can support large NAs with high efficiencies and no spherical aberration, owing to the exceptional scope of wavefront control afforded by the metasurface design and manufacturing process. Also, metalenses can be readily fabricated at wafer scales using mature nanofabrication foundry processes.

In this work, we use two sets of metalens arrays for parallel TPL fabrication (see Methods and Extended Data Fig. 1): a 50 × 50 lens array (200-μm lens, NA 1.0), which facilitates printing over an area of 1×1 cm^2 with exceptional high resolution, and a 370 × 350 lens array (100-μm lens, NA 0.8), which is designed to maximize parallel fabrication throughput. Both metalens arrays are designed using geometric phase, in which local phase response is specified by the angular orientation of rectangular meta-atom elements[31]. The meta-atom geometry is optimized to support accurate phase conversion and high transmission at 800 nm using parametric sweeps with rigorous coupled-wave analysis. Metalenses are tiled into arrays with 100% filling fraction and generate focal spots with spacings equal to their own sizes (200 μm or 100 μm), as illustrated in Fig. 1d and Extended Data Fig. 1c. A 3D full-wave simulation of the 200-μm, NA 1.0 metalens at 800 nm is presented in Fig. 1e and shows submicron-scale diffraction-limited focusing capabilities. We note that, owing to the spectral bandwidth of femtosecond pulses, chromatic dispersion can manifest with our basic metasurface designs and lead to point-spread-function broadening. These effects are discussed in the Supplementary Information and can be mitigated using advanced metasurface designs that support chromatic dispersion compensation[32,33].

Integration of the metalens array with the TPL optical system is illustrated in Fig. 1c and Extended Data Fig. 2. The metalens TPL system is powered by an ultrafast laser amplifier, which generates linearly polarized pulses at a central wavelength of 800 nm, a repetition rate of 1 kHz, a pulse width of 35 fs and an average power of 7 W. In the optical system, the laser beam is adjusted to a suitable operation power, expanded to fully fill the SLM aperture and then routed to a phase-to-amplitude optical module to enable greyscale intensity modulation (see Methods and Extended Data Fig. 3). The laser beam is then relayed to the metalens array printing head by means of a 4*f* system. As the ultrahigh-intensity (>10^{17} W cm^{-2}) femtosecond focal spot of the 4*f* system can ionize the air and disrupt the laser beam[34], we insert a vacuum cell with two flat windows at the intermediate focal plane to ensure high beam quality (Fig. 1c). A calibration process is performed using the SLM to account for and mitigate the non-uniform (Gaussian) intensity profile of the laser beam, metalens fabrication imperfections, and optical defects in the beam path (see Methods). After calibration, each focal spot can be independently switched 'on' or 'off' or be precisely tuned into arbitrary greyscale intensity values until the occurrence of beam path realignment or metalens array change.

By translating the substrate using the motion stage (speeds are marked in Supplementary Table 3) with active control over each focal spot, the metalens TPL system can fabricate arbitrary 3D microstructures/nanostructures by solidifying the 3D motion trajectories. The space between the print head and substrate is narrow as a result of the microscale focal lengths of the metalenses, making it important to manage viscous drag effects and shear forces on the printed structures during mechanical substrate motion. We formulate a resin with low viscosity (269 cP) and a large two-photon cross-section (855 GM) for all of our printing tasks, as described in the Supplementary Information.

To demonstrate precise greyscale intensity control in the metalens TPL system, we print a series of nanowires ranging from subdiffraction to diffraction-limited linewidths by fine-tuning the SLM values. Owing to the nonlinear nature of TPL, the printed feature size is dependent on the laser intensity in the subdiffraction regime (subthreshold), in which a smaller amount of monomer is polymerized at lower laser intensity[35]. Figure 1f and Extended Data Fig. 5 show a large array of suspended lines printed with high-power metalenses (NA = 1.0) at the subdiffraction regime, featuring a minimum lateral linewidth of 113 nm and axial linewidth of 262 nm. In a survey of linewidths (Fig. 1g, standard deviation = 16.5 nm, $n = 10$), we observe a low degree of variance in linewidths printed using different metalenses, which indicates a high degree of precision and consistency after SLM calibration and is instrumental to our parallel fabrication strategy. Figure 1h and Extended Data Fig. 6a–d show the continuous linewidth modulation by means of precise SLM greyscale control. Extended Data Fig. 6e,f shows the printing of 3D architectures using subthreshold laser power. As the laser intensity increases from subthreshold to above threshold, the linewidth converges to the laser focal spot size. We observe a highly robust printing window (Extended Data Fig. 6b) for the fabrication of features larger than the diffraction limit (>400 nm).

The capabilities and speed of our TPL printer are showcased in the fabrication of test structures spanning the full metalens array aperture. To demonstrate the ability to fabricate arbitrary 3D microstructures/nanostructures, we print a heterogeneous set of 3D microlattice cubes shown in Fig. 1i, each printed using an individual metalens. In Fig. 1j,k and Extended Data Fig. 4, we demonstrate the rapid fabrication (<2 h of printing time) of inch-scale logos (30 × 30 × 0.32 mm^3) of Lawrence

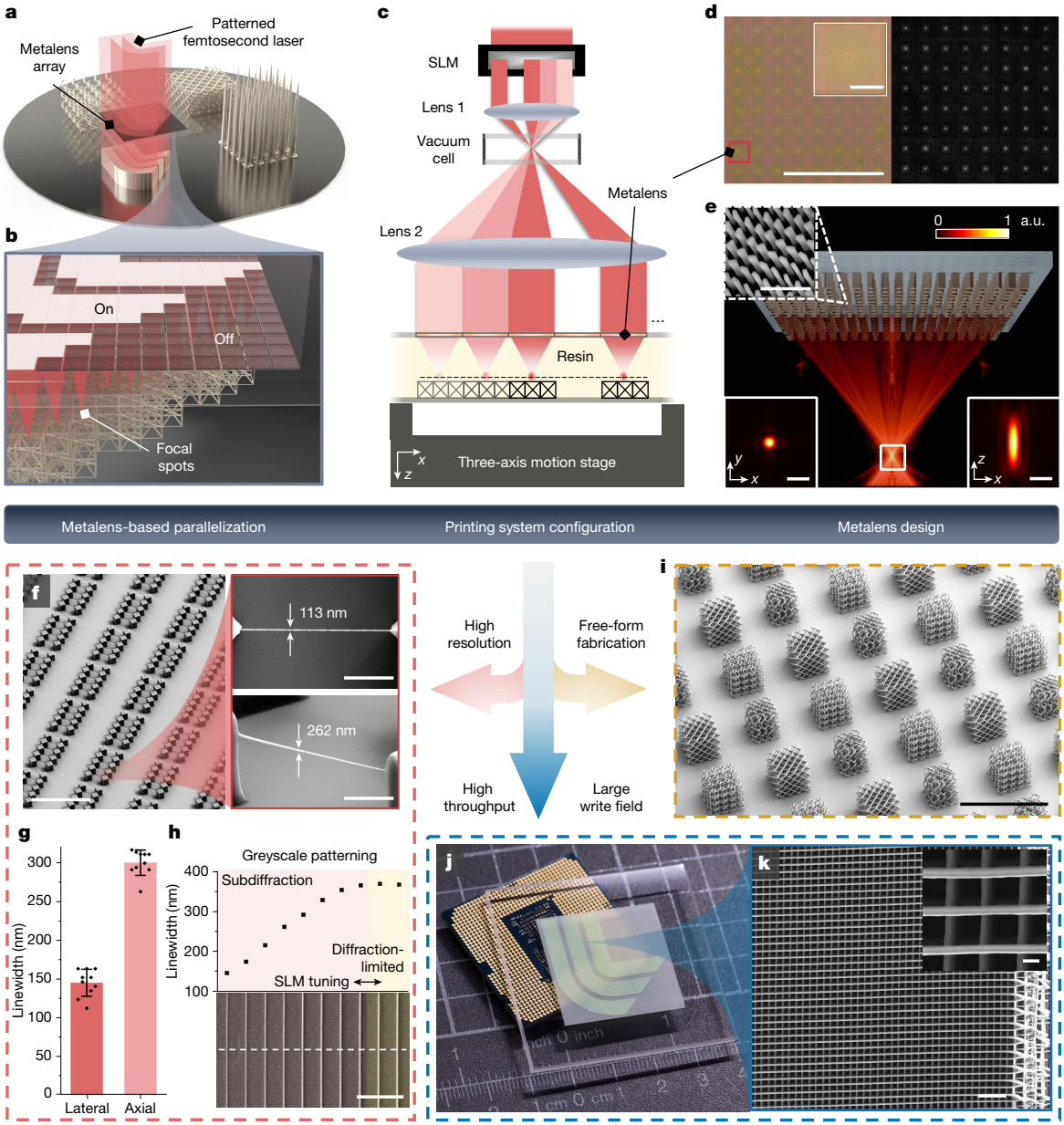

Fig. 1 | Metalens-based TPL. a,**b**, Schematic of metalens-based TPL: a patterned femtosecond laser is projected onto a metalens array to generate focal spots for parallel 3D nanolithography. **c**, The laser is patterned using an SLM, which is then projected onto a metalens array through lenses 1 and 2 to generate a focal spot array in the resin. A vacuum cell that prevents gas-phase ionization is inserted at the laser focal point in the 4*f* system. Each focal spot can be tuned to a desired greyscale intensity value. **d**, Optical microscope image of 100-µm, NA 0.8 metalenses and the generated focal spots. The focal spots are overexposed for clear visualization of focal spacing. Scale bars, 500 µm and 50 µm. **e**, Simulated point spread function of a 200-µm, NA 1.0 metalens. Top-left inset, scanning electron microscopy (SEM) image of the silicon nanostructures in the metalens. Bottom insets, zoomed-in views of the point spread function. Scale bars, 1 µm. The colour maps are normalized in dB scale for the main figure and in linear scale for the zoomed-in views. a.u., arbitrary units. **f**, Left, SEM image of an array of subdiffraction suspended nanowires written by 200-µm, NA 1.0 metalenses. Scale bar, 100 µm. Right, zoomed-in images showing the top and the 50° oblique view of a nanowire. Scale bars, 5 µm. **g**, A survey of linewidths of the printed nanowires. The linewidths are acquired by randomly picking nanowires printed by different metalenses and the error bars represent one standard deviation of the data. **h**, A nanowire array printed sequentially by a 200-µm, NA 1.0 metalens with precise greyscale tuning, showing subdiffraction and diffraction-limited feature printing capabilities. Scale bar, 10 µm. **i**, A series of 3D microlattice cubes printed by active modulation of the focal spot array. Scale bar, 500 µm. **j**, A LLNL logo printed using the 100-µm, NA 0.8 metalens array, placed next to a central processing unit chip. **k**, Zoomed-in SEM image of **j** showing the top layer structure: single-scan woodpile with sub-micrometre linewidth. Scale bar, 10 µm. Inset, further zoomed-in view showing well-resolved individual lines with 2.5-µm pitch. Scale bar, 1 µm.

Livermore National Laboratory (LLNL) and Stanford University with sub-micrometre linewidths. Such a task would take a serial-scan TPL machine more than a month to complete, with accumulated stitching defects and a high risk of error during the prolonged printing time.

We further fabricate a series of benchmark structures to showcase the printing quality and versatility of our method. As shown in Fig. 2, our parallel strategy excels in printing both replicated microstructures in arrays and continuously connected architectures. In Fig. 2a, we demonstrate the large-scale replication of microscale 3DBenchy[36] structures, which include overhanging, perforated and acute-angle features. The printed 3DBenchy array accurately replicates the original design. Figure 2b,c demonstrates the fabrication of

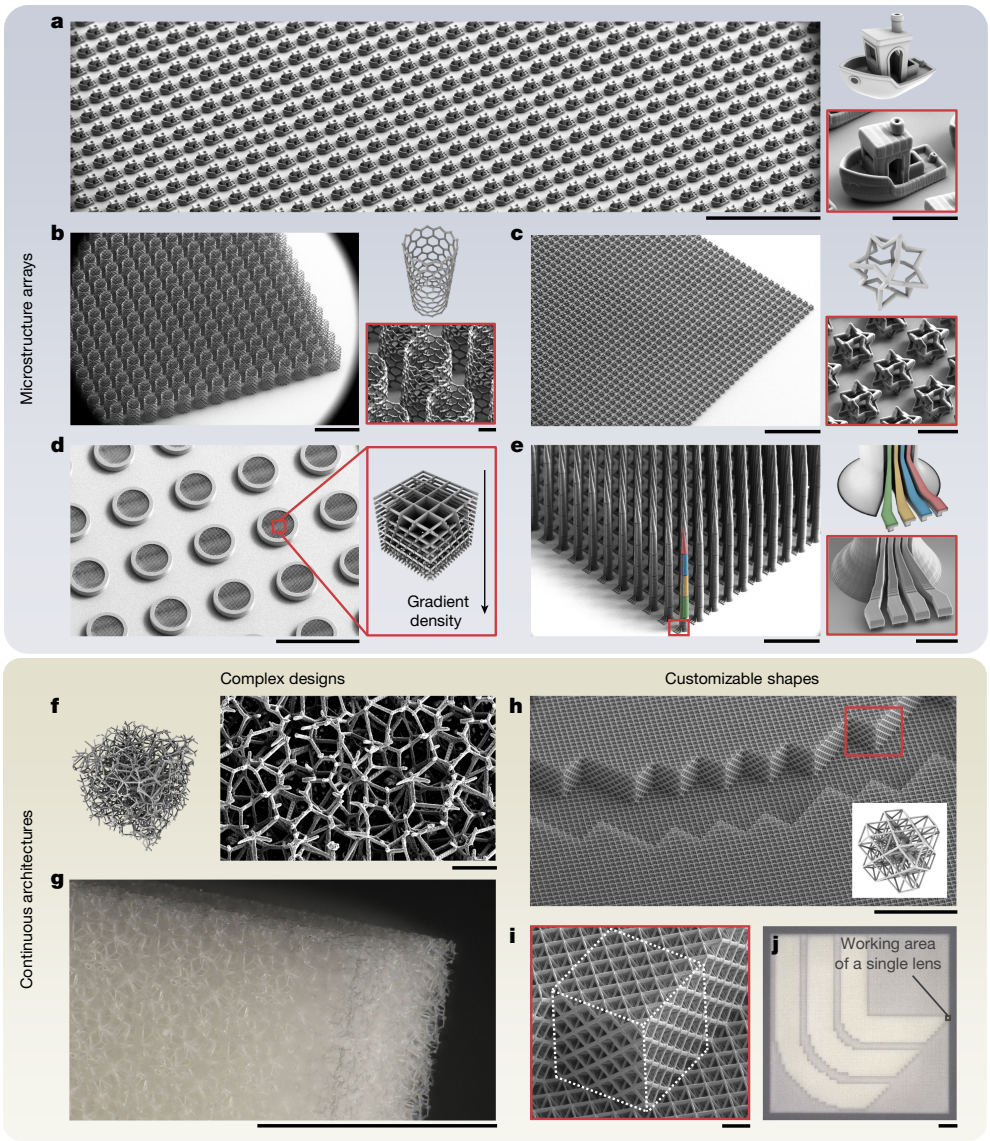

Fig. 2 | Parallel fabrication of microstructures/nanostructures. a, Scanning electron microscopy (SEM) image of a fleet of microscale boats (3DBenchy[36]) and a zoomed-in view for a single boat. Scale bars, 500 µm and 50 µm. **b**, SEM images of an array of carbon-nanotube-shaped microparticles. Scale bars, 500 µm and 50 µm. **c**, SEM images of an array of concave polyhedron microparticles. Scale bars, 500 µm and 50 µm. **d**, SEM images of a gradient-density foam laser target array. Scale bar, 500 µm. **e**, SEM images of a multiplexed microneedle array and a zoomed-in view of four wiring pads with undercut to provide electrical isolation after metal coating. The four independent probing zones are labelled in pseudo-colour in the SEM zoomed-out image and in the CAD design. Scale bars, 500 µm and 50 µm. **f**, Design and SEM image of a complex 3D Voronoi lattice structure. Scale bar, 50 µm. **g**, Optical image of the Voronoi structure in **f**. Scale bar, 500 µm. **h**, SEM image of a portion of a 1-cm^2 LLNL logo assembled by 50-µm octet units (4% density) showing minimal stitching errors and well-defined custom boundaries. Scale bar, 500 µm. **i**, Zoomed-in SEM image at the boundary of the lattice, in which a lattice cube printed with a single metalens is labelled. Scale bar, 50 µm. **j**, Optical image of the 1-cm^2 LLNL logo, in which the working area of a single metalens is labelled. Scale bar, 1 mm.

microparticles that are difficult to create using traditional methods, such as moulding. In the case of Fig. 2c, we fabricate 22.5k concave polyhedron microparticles (about 50 µm in size) within 0.5 h using the smaller high-resolution metalens array (2.5k lenses). The larger array with 120k metalenses boosts the fabrication rate for such particles to 50 M counts per day. Figure 2d shows the scalable fabrication of gradient-density foams, which have broad applications in laser-driven proton acceleration[5], gradient metamaterials[37] and photonic crystals[38]. In Fig. 2e and Supplementary Fig. 7, we fabricate a multidepth microneedle array that can potentially be applied as a 3D multiplexed neural interface[39].

Our concept further addresses and mitigates long-range stitching error, which is a feature in traditional TPL methods (Supplementary Fig. 8a,b) and leads to compromised mechanical properties, leakage and low surface quality. The error comes from several sources, such as low precision of long-range motion, scan-field distortion that causes misalignment with stage motion, and the shadowing effect, in which the previously printed sections block the laser beam and compromise beam quality when printing the neighbouring sections[40]. During the printing of each layer with our method, individual subsections printed by each focal spot, with an area equal to that of the metalens, will automatically and precisely stitch together across the entire processing area without any shadowing effects. Figure 2f–j and Supplementary Fig. 8d,e demonstrate the fabrication of centimetre-sized Voronoi lattices, octet lattices and woodpile structures with minimal stitching seams (<100 nm). As the input laser can be patterned by the SLM to turn off some focal spots, we design the laser pattern and fabricate an octet lattice structure with well-defined custom boundaries of a LLNL logo

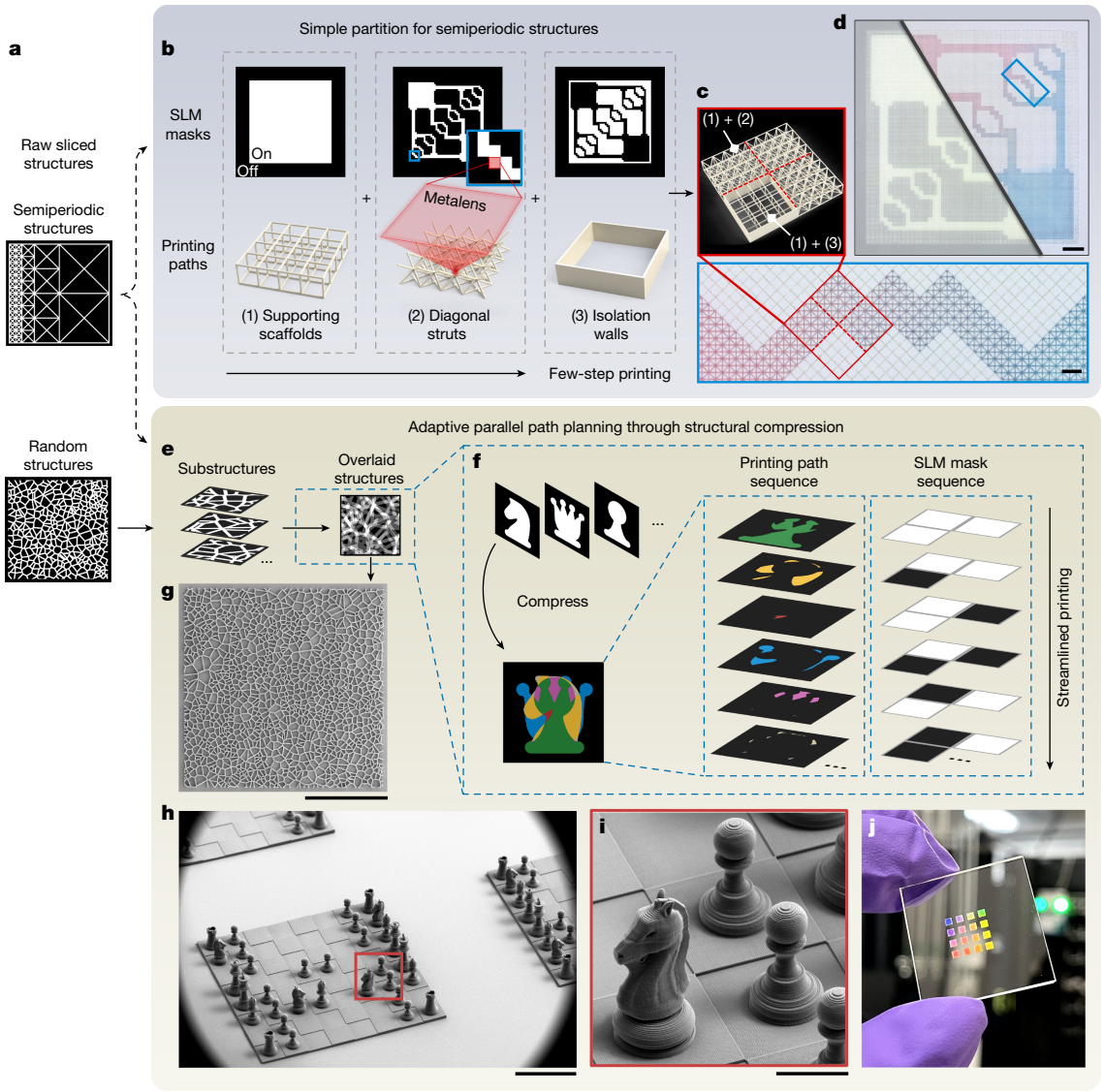

Fig. 3 | Adaptive parallelization strategies for complex structures. a, Example of two complex structures: semiperiodic and random lattice structures. Semiperiodic structures can be processed using either the partitioning method shown in the top-right box or the adaptive approach shown in the box below. Random structures can only be processed using the adaptive approach. **b**, Usual parallel printing strategy for a microcellular fluidic structure containing three different structures, that is, the supporting scaffolds, diagonal struts and isolation walls. **c**, Zoomed-in view of the cellular fluidic CAD model and the printed device showing a colour gradient after solvent evaporation. Scale bar, 100 µm. **d**, Left, as-fabricated structure under an optical microscope. Right, structure infused with diluted red and blue inks by drawing liquids from the two reservoirs through capillary action. Scale bar, 1 mm. **e**, Structure compression before adaptive parallel printing, in which the raw structure is segmented into substructures for each metalens. The substructures are combined to obtain an overlaid structure. **f**, Illustration of the structure compression process using simple 2D geometries (chess pieces) as the substructures, in which the overlapped regions and non-overlapped regions that correspond to different focal spot patterns are labelled in different colours. After compression, a sequence of printing paths and corresponding SLM masks are generated for parallel printing. **g**, SEM image of a 2D Voronoi lattice printed using adaptive parallelization. Scale bar, 500 µm. **h**, SEM image of a chess opening (London System) 3D structure printed using adaptive parallelization. Scale bar, 500 µm. **i**, Zoomed-in view of **h** showing individual chess pieces. Scale bar, 100 µm. **j**, Photo of 16 different chess openings over a 1-cm^2 area printed in parallel. The printed chess openings exhibit structural colouration under ambient light owing to the specific combination of the line spacing and printing resolution.

(Fig. 2h–j). This modulation method serves as our baseline strategy for fabricating structures that are not fully periodic.

Adaptive meta-lithography

To generalize the capabilities of metalens TPL, we develop two complementary approaches for printing semiperiodic and arbitrary 3D structures with on-demand parallelization through dynamic control of SLM during printing, as illustrated in Fig. 3. We define a semiperiodic structure as one consisting of a non-trivial global shape filled with periodic internal structure or of one containing a hierarchy of periodic shapes with different pitches or repeating geometries. For semiperiodic structures, an intuitive approach is to partition the processing volume and sequentially print sections with varying periodicity to obtain the final structure (Fig. 3b). As a demonstration, we fabricate a 1-cm^2 semiperiod microfluidic capillary network that emulates biological vascular networks using this method. In this device, two liquids are added to the loading pads at opposite corners and driven by capillary forces into increasingly small channels, which eventually mix at the intersections (Fig. 3c,d and Supplementary Video 1).

Such open-to-environment cellular fluidic devices have many lab-on-a-chip applications in liquid transpiration, multiphase reaction and selective functionalization[41].

The entire device can be decomposed into a superposition of three sets of semiperiodic structures, each using a distinct SLM mask pattern for printing: a cubic lattice serving as supporting scaffolds, diagonal struts to guide liquid flow within the capillary channels, and isolation walls to better contain the liquid in the non-wetted areas. During the writing of each layer, detailed slice patterns and SLM masks corresponding to each of the three semiperiodic structures are exposed in sequence. To characterize the printed device, red and blue dyed liquid is injected into each loading pad (25% v/v isopropanol in water) and then dried. Figure 3c shows a zoomed-in view of the dried, transitional colour gradient that is spontaneously formed in the capillary channels in which the two liquids exchange chemical species.

To 3D-print fully aperiodic structures, we introduce a three-step adaptive meta-lithography (AML) method that optimizes print area segmentation and print path planning. First, the entire structure is segmented into individual substructures that match the cross-sectional area of an individual metalens (Fig. 3e). Second, similarities across all or subsets of the substructures are identified to compress the total toolpath and maximize throughput. Third, the substrate is mechanically scanned over the toolpath of the compressed structure with active focal spot control to produce the desired 3D structure. This printing strategy is general and applicable to a wide range of parallel fabrication systems equipped with several printing heads.

To illustrate this adaptive parallel path planning process, we use a simplified 2D representation in the shape of chess pieces for explanation purpose in Fig. 3f. Overlaid images of individual substructures reveal their 'compressibility', that is, the presence of features that can be printed simultaneously by specific subsets of focal spots. Next, a series of printing paths is generated on the basis of the overlaid pattern, with each printing path corresponding to a unique SLM mask pattern. The metalens TPL system sequentially executes these unique printing paths and SLM patterns to minimize the instances of SLM refreshing, which is particularly important for us owing to the low refresh rate (60 Hz) of our SLM. Extended Data Fig. 7 illustrates the throughput scaling of metalens TPL using AML (see Methods). Using this strategy, we fabricate 2D patterns such as a number array and a fully random lattice structure (Supplementary Fig. 9 and Fig. 3g). We also use AML to print fully aperiodic 3D structures, including a set of 16 different chess openings over a 1-cm^2 area in one parallel process, with each chess piece printed by a single metalens (Fig. 3h–j and Supplementary Fig. 10), proving that it can efficiently print shared features while also individually addressing unique features in all substructures from arbitrary 3D structures.

Fabrication of functional metamaterials

In this work, we showcase the fabrication and characterization of large-scale mechanical (Fig. 4 and Extended Data Figs. 8 and 9) and electromagnetic terahertz (THz) metamaterials (see details in Methods and Extended Data Fig. 10), demonstrating how our ability to scale the nanoprinting process can lead to the discovery of new metamaterial phenomena. Metamaterials are artificially structured media with macroscopic physical properties that are based on the rational design of their internal nanoscale and microscale architectures, but their detailed investigation so far has been limited to microscale structures manufactured using conventional TPL techniques. Metalens TPL provides an ideal platform to scale-up metamaterial fabrication and, in doing so, unlocks new regimes in the study and implementation of large-scale functional metamaterial systems.

Mechanical metamaterials have shown intriguing properties, such as light weight, high strength and toughness, and programmable responses[42]. However, it has not been possible to study their fracture and crack growth behaviours at macroscopic scales owing to the limited throughput and substantial stitching errors of conventional TPL methods. We design and fabricate macroscale mechanical metamaterials featuring three distinct types of microarchitecture: stretching-dominated octet lattices, bending-dominated Kelvin lattices[43] and interlocked but not rigidly connected chainmail lattices[12]. The three different lattices are in the shape of 10 × 5 × 0.6-mm^3 slabs consisting of 240,000 unit cells (unit size: 50 μm, 4% relative density). The chainmail lattices investigated here are a special case of polycatenated architected materials[12] and they consist of vertically stacked polyhedron cages (across 0.6 mm thickness) that are interlocked along the lateral directions. To understand crack propagation during fracture, we add a one-unit-cell wide and 1.6-mm-long notch at the centre of each lattice sample by active SLM modulation during printing (Fig. 4a–c).

We conduct uniaxial tensile experiments using a custom in situ micromechanical testing system (illustrated in Fig. 4a–c; see Methods). The tensile test results of several samples for each type of lattice are summarized in Fig. 4d. The octet lattices exhibit the highest stiffness, as expected, and they fracture catastrophically at a displacement of about 320 μm. The Kelvin lattices have a lower stiffness than the octet lattices and exhibit a slightly longer displacement (approximately 362 μm) at peak stress, followed by a relatively slower crack propagation. By strong contrast, the chainmail lattices can dynamically rearrange the positions of their interlocked unit cells, resulting in a much larger displacement (about 1,914 μm) at peak stress, followed by gradual crack propagation with alternating breakage of interlocked unit cells at the two ends of the notch. The chainmail lattices exhibit a much higher toughness against fracture with an energy to fracture of 216.9 J m^{-2}, compared with that of 153.2 J m^{-2} for the octet lattices and 87.9 J m^{-2} for the Kelvin lattices.

To further understand these distinct fracture behaviours, we conduct hybrid finite element modelling (FEM) for the octet and Kelvin lattices and level set discrete element modelling (LS-DEM) for the chainmail lattices (see Methods). The hybrid FEM model treats the overall lattice structures as a homogenized medium with properties defined by the unit-cell geometry, whereas the region near the notch tip is explicitly modelled as discrete beams (Extended Data Fig. 9). For the octet and Kelvin lattices, the simulated shape of the notch tip before fracture matches well with the in situ tensile experiments (Fig. 4g,h and Supplementary Video 2). These simulations reveal the plastic zone size of both the octet and Kelvin lattices to be much smaller than the sample size, as labelled in Fig. 4f,i. As a result, largely brittle failures occur for both lattices[44], as shown in the fractured surfaces in Fig. 4e,j.

On the other hand, the LS-DEM model qualitatively explains the toughening mechanisms of the chainmail lattices owing to their unique interlocking nature. Supplementary Video 3 shows that LS-DEM simulation captures the dynamic rearrangement and crack opening phenomena as seen in the in situ tensile experiments. Three snapshots of the simulation are presented in Fig. 4k, with each particle coloured by normalized stress. The LS-DEM model reveals that, unlike the octet and Kelvin lattices in which stress is concentrated at the crack tip, the chainmail lattices distribute the stress over chains of load-bearing unit cells along the tensile loading direction. As the crack propagates, the interlocked unit cells at the crack tip are broken apart, which triggers immediate adjustment in the spatial arrangement and stress distribution of many surrounding unit cells. This dynamic rearrangement owing to mechanical interlocking leads to highly ductile crack propagation with alternating advancement of two crack tips, as seen in Supplementary Videos 2 and 3.

Discussion and outlook

A summary of frontier developments in TPL and other relevant high-resolution AM methods is presented in Fig. 5a,b, which highlights

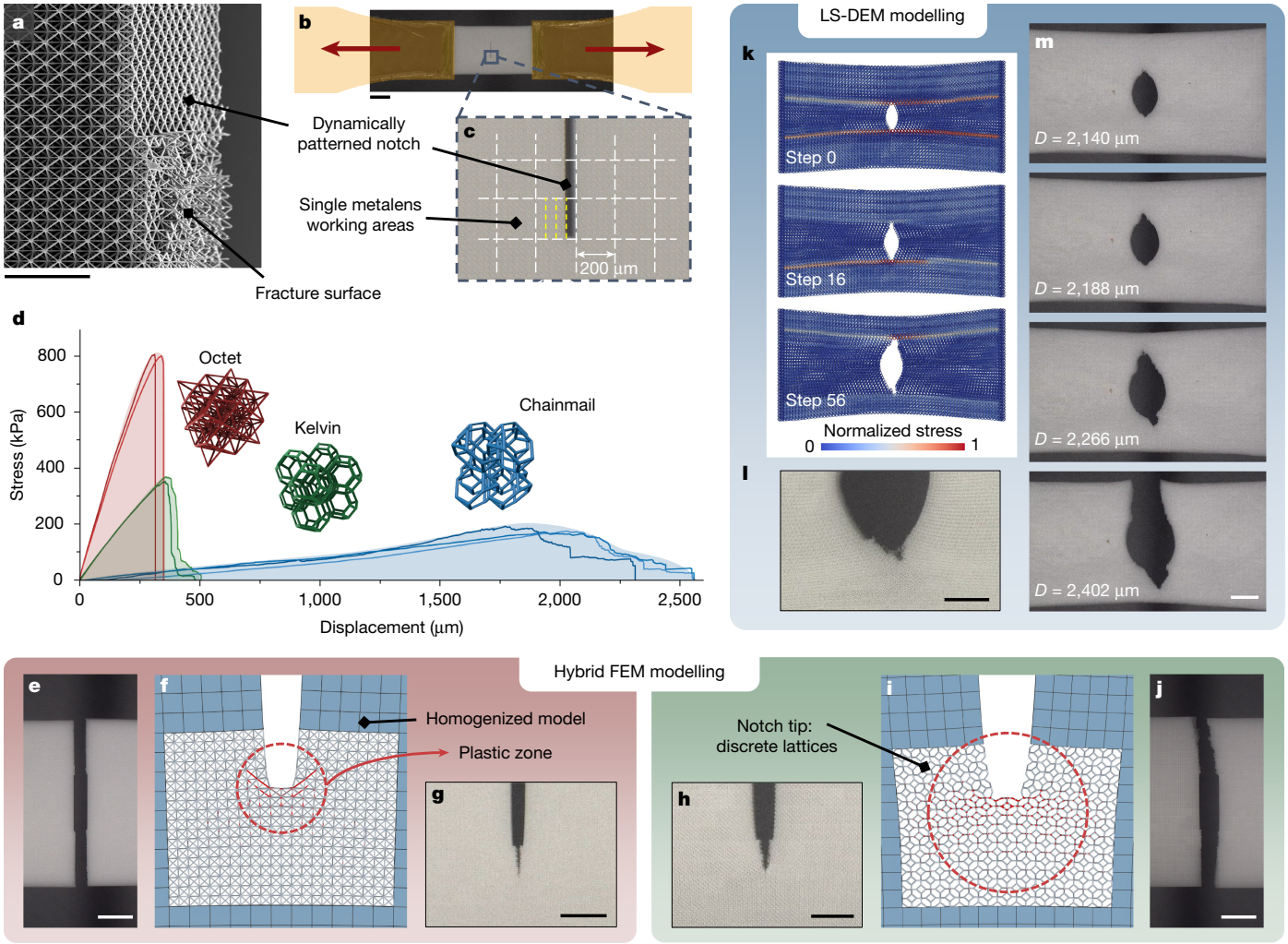

Fig. 4 | Fabrication and tensile testing of large-scale mechanical metamaterials. a, SEM image of a tensile-tested octet structure showing the notch zone and fracture surface. Scale bar, 200 µm. **b**, Schematic of the tensile test, in which the gripping ends are attached to the lattice structures to form a dogbone-shaped specimen. Scale bar, 1 mm. **c**, Zoomed-in optical image of **b** showing the narrow notch opening and the working area for each metalens ($200 \times 200\ \mu m^2$). The laser is dynamically patterned during printing to form the notch opening narrower than the metalens size. **d**, Stress–displacement curves measured for the octet, Kelvin and chainmail lattices. **e**, Optical image of a fractured octet lattice. Scale bar, 1 mm. **f**, Equivalent stress contour plot of hybrid FEM simulation for the octet lattice (average element stress). Stress above yield (100 MPa) is represented in red. The approximate plastic zone is marked with a red circle. **g**, Optical image of the octet lattice during crack initiation. Scale bar, 500 µm. **h**, Optical image of the Kelvin lattice during crack initiation. Scale bar, 500 µm. **i**, Equivalent stress contour plot of hybrid FEM simulation for the Kelvin lattice (elemental difference stress). Stress above yield (100 MPa) is represented in red. The approximate plastic zone is marked with a red circle. **j**, Optical image of a fractured Kelvin lattice. Scale bar, 1 mm. **k**, LS-DEM modelling to visualize the crack propagation for the chainmail lattice. **l**, Optical image of the chainmail lattice during crack initiation. Scale bar, 500 µm. **m**, Optical image series showing the crack propagation of the chainmail lattice. Scale bar, 1 mm.

the intrinsic trade-off between peak printing throughput, minimum feature size and lateral write field area. Our inclusion of write field area here is essential in assessing the future scaling potential of TPL methods and their ability to print macroscopic structures. This analysis is distinctive from most previous works that focus solely on the trade-off between the peak throughput and feature size, as reflected in the commonly used speed–resolution chart (Fig. 5a). We observe in Fig. 5b that past works have demonstrated high peak throughputs of about 10^8 voxels s^{-1}. However, these works are also generally constrained by bounds specified by the FOV and proximity constraints, which set limits to write field area and throughput, respectively. The FOV constraint arises because of the limited FOV of conventional microscope objective lenses used in conventional TPL concepts, which spans hundreds of micrometres per lateral dimension[13,14,18,19,21]. The proximity constraint is a gradient function determined by factors including the write field volume, the voxel size and the minimum spacing between focal spots. For parallel TPL methods that feature a large number of focal spots, we estimate a voxel spacing limitation near 10 µm, below which adjacent focal spots start to exhibit strong crosstalk that induces undesired polymerization and overgrowth[14,22] (Fig. 5c; see the Supplementary Information for discussion). To print large parts with conventional methods, entire structures are split into small sub-parts that can be fitted into the objective FOV and printed sequentially. Under this scenario, repetitive stage positioning becomes time-consuming, especially for high-throughput printing systems at $>10^7$ voxels s^{-1}. This extra throughput penalty is illustrated in Fig. 5d and discussed in the Supplementary Information. Also, these long-range field stitching methods can lead to stitching defects that compromise the surface quality and mechanical performance[14] (Fig. 5e and Supplementary Fig. 8).

By contrast, our parallel metalens TPL concept presents a qualitatively different approach to 3D nanolithography and offers a

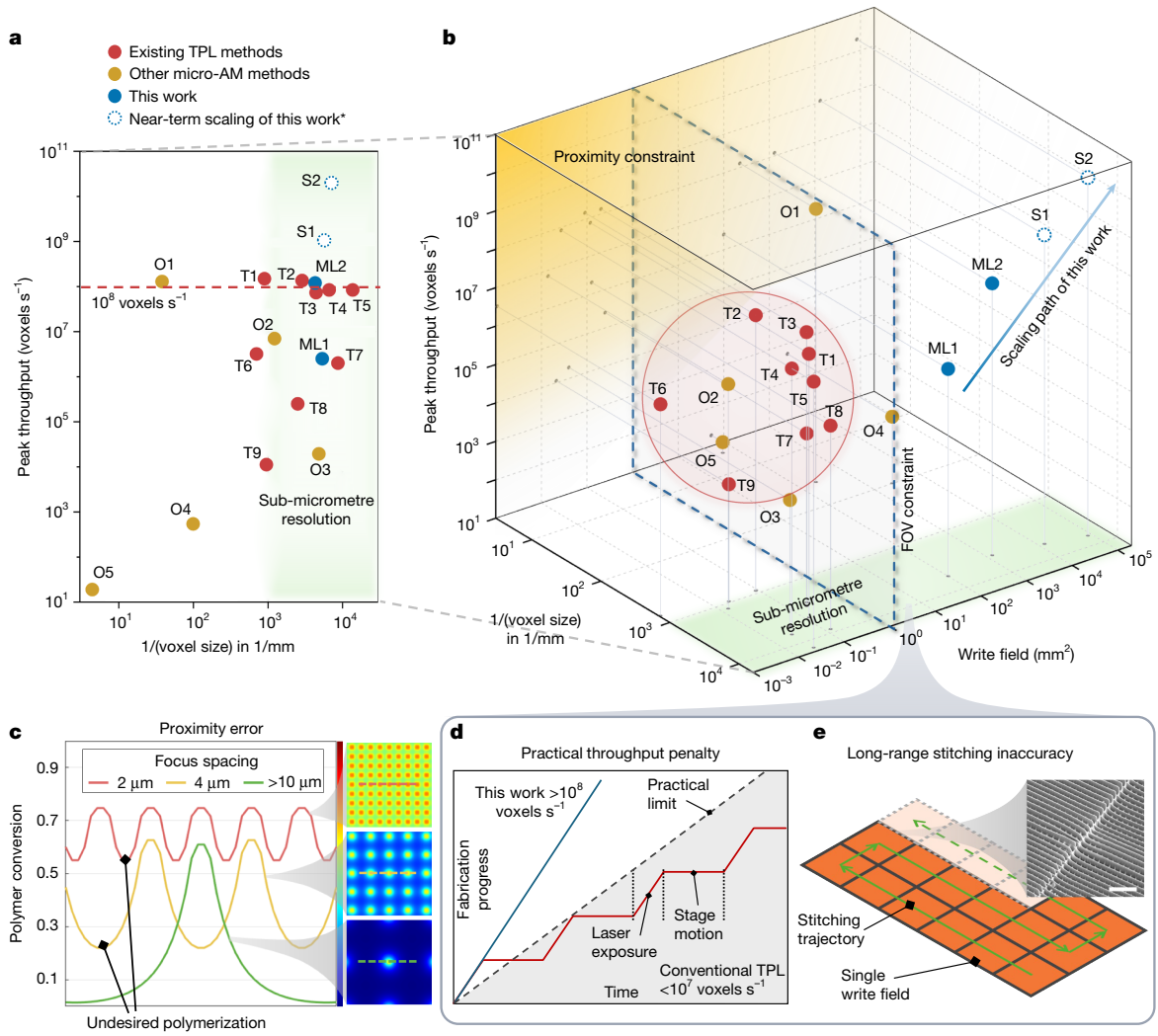

Fig. 5 | Throughput scaling of 3D lithography technologies. a, 2D chart comparing the peak fabrication throughput and the voxel size of existing micro-AM techniques. T1–T9: existing TPL techniques. O1–O5: other high-precision AM techniques. ML1: 50 × 50 metalens array, NA 1.0, size 200 µm. ML2: 350 × 370 metalens array, NA 0.8, size 100 µm. S1 and S2: near-term scaling of this work. *The near-term scaling is intended for future development based on commercially available components, as discussed in the Supplementary Information. Literature references: T1: 2023, Jiao et al.[21]; T2: 2024, Zhang et al.[18]; T3: 2024, Kiefer et al.[19]; T4: 2019, Saha et al.[14]; T5: 2022, Han et al.[13]; T6: 2021, Somers et al.[15]; T7: 2023, Ouyang et al.[17]; T8: Nanoscribe Photonic Professional GT2, datasheet[47]; T9: 2019, Geng et al.[16]; O1: 2024, Vidler et al.[7]; O2: 2022, Hahn et al.[48]; O3: 2021, Hahn et al.[49]; O4: 2016, Zheng et al.[50]; O5: 2022, Sanders et al.[8]. **b**, 3D chart comparing the peak fabrication throughput, voxel size and lateral write field area. Bounds specifying FOV and proximity error constraints that are typical of existing methods are specified. **c**–**e**, Fundamental challenges posed by TPL methods using microscope objective lenses. **c**, Undesired polymerization caused by the proximity of adjacent focal spots. This chart simulates the polymer conversion under a given laser exposure condition with different focal spot spacing. See the Supplementary Information for more details. **d**, Practical fabrication throughput for large structures through the sequential stitching of sub-1-mm^2 write fields, indicating a practical throughput limit for conventional TPL methods at about 10^7 voxels s^{-1}. See the Supplementary Information for more details. **e**, Defects caused by long-range sequential stitching during the printing of a large part. The SEM image shows stitching defects in a woodpile structure printed using a commercial TPL printer. Scale bar, 10 µm. See the Supplementary Information for details.

straightforward and, in principle, unconstrained strategy to scaling up TPL. In its current form as prototyped, our system already achieves an ultrahigh fabrication throughput, high resolution, centimetre-scale write field area and the capability of printing aperiodic structures. The throughput metrics for our system using the two metalens arrays (50 × 50, 200-µm lens, NA 1.0 and 370 × 350, 100-µm lens, NA 0.8) are plotted in Fig. 5a,b and show a peak throughput of 1.2×10^8 voxels s^{-1} over a write field area of 12 cm^2. We anticipate that this scaling concept can surpass 10^{10} voxels s^{-1} with improved optics such as larger optics and metalens arrays, advanced SLM technologies, and ultrafast lasers featuring higher pulse energies and higher repetition rates (>10 kHz) than this work. We marked the near-term throughput scaling on the basis of commercially available components in Fig. 5a,b, with details discussed in the Supplementary Information.

A key challenge of the projected scaling is the handling of the substantial amount of information embedded in large, complex 3D structures, which we face in this work. Similar data bottlenecks had emerged in 2D maskless lithography and were addressed with extensive efforts in layout compression algorithms and data preparation methods[45,46]. As such, we anticipate that the development of advanced data representation, processing and storage for large, complex 3D architectures will benefit such parallel fabrication methods from the large library of technologies in data compression, parallel computation and deep learning. We foresee the future of 3D nanolithography as massively parallel, swiftly adaptive and computationally agile, enabling the transformative and practical use of nanoarchitected materials across diverse fields, including microelectronics, biomedicine, high-energy laser target, quantum information processing and beyond.

Online content

Any methods, additional references, Nature Portfolio reporting summaries, source data, extended data, supplementary information, acknowledgements, peer review information; details of author contributions and competing interests; and statements of data and code availability are available at https://doi.org/10.1038/s41586-025-09842-x.

1. Kawata, S., Sun, H. B., Tanaka, T. & Takada, K. Finer features for functional microdevices. *Nature* **412**, 697–698 (2001).
2. Kim, S., Kubicek, R. & Bergbreiter, S. 3D-printed electrostatic microactuators for flexible microsystems. *Adv. Funct. Mater.* **33**, 202304991 (2023).
3. Urciuolo, A. et al. Intravital three-dimensional bioprinting. *Nat. Biomed. Eng.* **4**, 901–915 (2020).
4. Xu, S. et al. 3D-printed micro ion trap technology for quantum information applications. *Nature* **645**, 362–368 (2025).
5. Qin, C. et al. High efficiency laser-driven proton sources using 3D-printed micro-structure. *Commun. Phys.* **5**, 124 (2022).
6. Jiang, L. J., Campbell, J. H., Lu, Y. F., Bernat, T. & Petta, N. Direct writing target structures by two-photon polymerization. *Fusion Sci. Technol.* **70**, 295–309 (2017).
7. Vidler, C. et al. Dynamic interface printing. *Nature* **634**, 1096–1102 (2024).
8. Sanders, S. N. et al. Triplet fusion upconversion nanocapsules for volumetric 3D printing. *Nature* **604**, 474–478 (2022).
9. Jung, W. et al. Three-dimensional nanoprinting via charged aerosol jets. *Nature* **592**, 54–59 (2021).
10. Kronenfeld, J. M., Rother, L., Saccone, M. A., Dulay, M. T. & DeSimone, J. M. Roll-to-roll, high-resolution 3D printing of shape-specific particles. *Nature* **627**, 306–312 (2024).
11. Xia, X. et al. Electrochemically reconfigurable architected materials. *Nature* **573**, 205–213 (2019).
12. Zhou, W. et al. 3D polycatenated architected materials. *Science* **387**, 269–277 (2025).
13. Han, F. et al. Three-dimensional nanofabrication via ultrafast laser patterning and kinetically regulated material assembly. *Science* **378**, 1325–1331 (2022).
14. Saha, S. K. et al. Scalable submicrometer additive manufacturing. *Science* **366**, 105–109 (2019).
15. Somers, P. et al. Rapid, continuous projection multi-photon 3D printing enabled by spatiotemporal focusing of femtosecond pulses. *Light Sci. Appl.* **10**, 199 (2021).
16. Geng, Q., Wang, D., Chen, P. & Chen, S. C. Ultrafast multi-focus 3-D nano-fabrication based on two-photon polymerization. *Nat. Commun.* **10**, 2179 (2019).
17. Ouyang, W. et al. Ultrafast 3D nanofabrication via digital holography. *Nat. Commun.* **14**, 1716 (2023).
18. Zhang, L. et al. High-throughput two-photon 3D printing enabled by holographic multi-foci high-speed scanning. *Nano Lett.* **24**, 2671–2679 (2024).
19. Kiefer, P. A multi-photon (7 × 7)-focus 3D laser printer based on a 3D-printed diffractive optical element and a 3D-printed multi-lens array. *Light Adv. Manuf.* **4**, 28–41 (2024).
20. Yang, S. et al. Parallel two-photon lithography achieving uniform sub-200 nm features with thousands of individually controlled foci. *Opt. Express* **31**, 14174–14184 (2023).
21. Jiao, B. et al. Acousto-optic scanning spatial-switching multiphoton lithography. *Int. J. Extreme Manuf.* **5**, 035008 (2023).
22. Arnoux, C. et al. Understanding and overcoming proximity effects in multi-spot two-photon direct laser writing. *Add. Manuf.* **49**, 102491 (2022).
23. Wang, X. et al. 3D nanolithography via holographic multi-focus metalens. *Laser Photonics Rev.* **18**, 2400181 (2024).
24. Walsh, M. E., Zhang, F., Menon, R. & Smith, H. I. in *Nanolithography* (ed. Feldman, M.) 179–193 (Woodhead Publishing, 2014).
25. Sugioka, K. & Cheng, Y. Femtosecond laser three-dimensional micro- and nanofabrication. *Appl. Phys. Rev.* **1**, 041303 (2014).
26. Gu, S., Chen, B., Xu, X., Han, F. & Chen, S. C. 3D nanofabrication via directed material assembly: mechanism, method, and future. *Adv. Mater.* **37**, 2312915 (2025).
27. Khorasaninejad, M. & Capasso, F. Metalenses: versatile multifunctional photonic components. *Science* **358**, eaam8100 (2017).
28. Arbabi, A., Horie, Y., Bagheri, M. & Faraon, A. Dielectric metasurfaces for complete control of phase and polarization with subwavelength spatial resolution and high transmission. *Nat. Nanotechnol.* **10**, 937–943 (2015).
29. Fu, J. et al. Supercritical metalens at h-line for high-resolution direct laser writing. *Opto-Electron. Sci.* **3**, 230035 (2024).
30. Chen, B. et al. 4H-SiC metalens: mitigating thermal drift effect in high-power laser irradiation. *Adv. Mater.* **37**, 2412414 (2025).
31. Zhou, Y., Mao, C., Gershnabel, E., Chen, M. & Fan, J. A. Large-area, high-numerical-aperture, freeform metasurfaces. *Laser Photonics Rev.* **18**, 2300988 (2024).
32. Li, Z. et al. Meta-optics achieves RGB-achromatic focusing for virtual reality. *Sci. Adv.* **7**, eabe4458 (2021).
33. Chen, W. T. et al. A broadband achromatic metalens for focusing and imaging in the visible. *Nat. Nanotechnol.* **13**, 220–226 (2018).
34. Zhang, L., Liu, J., Gong, W., Jiang, H. & Liu, S. Diffraction based single pulse measurement of air ionization dynamics induced by femtosecond laser. *Opt. Express* **29**, 18601–18610 (2021).
35. Fischer, J. & Wegener, M. Three-dimensional optical laser lithography beyond the diffraction limit. *Laser Photonics Rev.* **7**, 22–44 (2013).
36. 3DBenchy. https://www.3dbenchy.com/ (2024).
37. Zhang, P. et al. Mechanical design and energy absorption performances of rational gradient lattice metamaterials. *Compos. Struct.* **277**, 114606 (2021).
38. Liu, Y. et al. Structural color three-dimensional printing by shrinking photonic crystals. *Nat. Commun.* **10**, 4340 (2019).
39. Wang, P. et al. Direct-print 3D electrodes for large-scale, high-density, and customizable neural interfaces. *Adv. Sci.* **12**, 2408602 (2025).
40. Dehaeck, S., Scheid, B. & Lambert, P. Adaptive stitching for meso-scale printing with two-photon lithography. *Addit. Manuf.* **21**, 589–597 (2018).
41. Dudukovic, N. A. et al. Cellular fluidics. *Nature* **595**, 58–65 (2021).
42. Jiao, P., Mueller, J., Raney, J. R., Zheng, X. & Alavi, A. H. Mechanical metamaterials and beyond. *Nat. Commun.* **14**, 6004 (2023).
43. Gibson, L. J. & Ashby, M. F. *Cellular Solids* 2nd edn (Cambridge Univ. Press, 2014).
44. Patel, Z. S., Alrashed, A. O., Dwivedi, K., Salviato, M. & Meza, L. R. Rethinking ductility—a study into the size-affected fracture of additively manufactured polymers. *Addit. Manuf.* **84**, 104113 (2024).
45. Dai, V. & Zakhor, A. in *Emerging Lithographic Technologies IV* Vol. 3997, 467–477 (SPIE, 2000).
46. Liu, H.-I., Dai, V., Zakhor, A. & Nikolic, B. in *Emerging Lithographic Technologies X* Vol. 6151, 632–645 (SPIE, 2006).
47. Nanoscribe Photonic Professional GT2. https://www.nanoscribe.com/en/products/photonic-professional-gt2/ (2025).
48. Hahn, V. et al. Light-sheet 3D microprinting via two-colour two-step absorption. *Nat. Photon.* **16**, 784–791 (2022).
49. Hahn, V. et al. Two-step absorption instead of two-photon absorption in 3D nanoprinting. *Nat. Photon.* **15**, 932–938 (2021).
50. Zheng, X. et al. Multiscale metallic metamaterials. *Nat. Mater.* **15**, 1100–1106 (2016).

Publisher's note Springer Nature remains neutral with regard to jurisdictional claims in published maps and institutional affiliations.

Springer Nature or its licensor (e.g. a society or other partner) holds exclusive rights to this article under a publishing agreement with the author(s) or other rightsholder(s); author self-archiving of the accepted manuscript version of this article is solely governed by the terms of such publishing agreement and applicable law.

© The Author(s), under exclusive licence to Springer Nature Limited 2025

Methods

Metalens design and fabrication

Two different metalens arrays are used in this work: (1) 50 × 50, 200-μm lens, NA 1.0 and (2) 370 × 350, 100-μm lens, NA 0.8.

Extended Data Fig. 1 shows the design and fabrication of the metalens arrays. Geometric-phase-based metalenses are designed using rigorous coupled-wave analysis with the software package RETICOLO[51]. The optimal design obtained for h = 785 nm thick silicon embedded in hydrogen silsesquioxane (HSQ) (refractive index = 1.45) is with period Λ = 300 nm, length l = 195 nm and width w = 104 nm, which gives accurate phase conversion of 99.8% and transmission of 88.4% for each meta-atom. Full-wave simulations of both lenses are conducted using the finite difference time domain method with Tidy3D on cloud GPUs. Near-field responses for the metalens have been simulated with overall size up to 200 × 200 × 2.6 μm^3 with a spatial resolution of 32 nm. The near-field electromagnetic wave response after the metalens is obtained, which is then propagated to the far field in the x–y and x–z cross-sections to obtain the steady-state frequency domain solution. The simulated focal spot is compared with the focal spot of an ideal lens with the same square aperture, obtained with accurate vectorial diffraction using Stratton–Chu formula. The Strehl ratio for the simulation result is 0.87. The full wave at half maximum of the focus is simulated to be 385 nm (lateral) and 1.70 μm (axial). The result is included in Fig. 1e.

For the 50 × 50, 200-μm, NA 1.0 metalens array, 785-nm-thick polycrystalline silicon films are deposited on 4-inch fused silica substrates using low-pressure chemical vapour deposition. After dicing the wafer into 1-inch-square pieces, nanopatterns are written using electron-beam lithography with 14% HSQ in methyl isobutyl ketone as resist, with a conductive layer of Electra 92 and developed in 25% tetramethylammonium hydroxide. To reduce electron-beam lithography time, the beam current was set to 100 nA. The pattern is transferred to silicon using inductively coupled plasma reactive ion etching with Cl_2 and HBr. The etched device is embedded in 20% HSQ with a total thickness of 1.2 μm. Rapid thermal annealing at up to 1,100 °C was used to release the stress within HSQ films, without which the film is prone to cracking[52].

The 370 × 350, 100-μm, NA 0.8 metalens array was purchased from 2Pi Optics Inc. It has the same geometric phase metalens design and is produced by a custom nanofabrication recipe. The metalens is protected under a thin layer of SU-8.

Metalens-based TPL system

Extended Data Fig. 2 shows the schematic and photo of the metalens-based TPL system. An amplified femtosecond laser (Solstice, Spectra-Physics, wavelength 800 nm, average power 7 W, repetition rate 1 kHz, pulse width 35 fs) first passes through a half-wave plate (HWP1) and a high-power polarization beam splitter (PBS1) to modulate its average power. It is then expanded and collimated by a custom beam expander consisting of a concave lens (f = −100 mm) and a convex lens (f = 250 mm). After beam expansion, the size of the laser beam is large enough to fully fill the aperture of the SLM (X15213-02R, Hamamatsu). The expanded laser beam is then routed into an intensity modulator composed of an SLM, a quarter-wave plate (QWP1) and another polarization beam splitter (PBS2), to shape laser intensity profile, realizing flat-top or arbitrarily patterned beam (Extended Data Fig. 3). The patterned laser beam is then projected onto the metalens array to form a focal spot array, in which the SLM plane is in conjugation with the metalens array by a 4f system, allowing the SLM greyscale pattern to be accurately projected to the metalens plane. A vacuum chamber is inserted at the centre of the 4f system to prevent the intermediate focal spot from ionizing the air owing to the high pulse energy. Here there is another quarter-wave plate (QWP2) owing to the design of the metalens, which only focuses left-handed circularly polarized light. A microscope is placed on the other side of the metalens to monitor the printing process. The metalens and the printing substrate are both mounted on kinematic bases to adjust their relative pitch and roll relative to the motion stage. During printing, the photoresist is sandwiched between the metalens and the printing substrate and an XYZ motion stage (ANT130XY and ANT95LZ, Aerotech) is used to scan the printing substrate, in synchronization with the laser exposure to create 3D structures. Owing to the short travel range in the printing process (size of a metalens: ≤200 μm), a piezoelectric stage with sub-10-nm precision and kilohertz dynamic response can be used for the best scanning precision.

For the two metalens arrays, two different 4f systems are used to adjust the beam size to match the SLM pixel to the metalens size. For the 50 × 50, 200-μm, NA 1.0 metalens array, a 200-mm:200-mm lens pair is used to realize a 1:1 magnification ratio. As the SLM pixel size is 12.5 μm, each metalens is projected with 16×16 = 256 pixels. For the 370 × 350, 100-μm, NA 0.8 metalens array, a 75 mm:200 mm lens pair is used to realize a 1:2.667 magnification ratio. Each metalens is projected with 3 × 3 = 9 pixels.

For regular optics such as mirrors, lenses, waveplates and beam splitters, all of them have corresponding anti-reflection coatings at 800 nm, yielding an efficiency of >99% for each component. The SLM has an efficiency of >97% and the metalenses have a focusing efficiency of 62.2% (simulation) and 49.3% (experiment, possibly because of fabrication imperfections).

Principle of using SLM for laser patterning

The intensity modulation of the laser beam is accomplished using the configuration depicted in Extended Data Fig. 3. Before entering the intensity modulator, the femtosecond laser is in vertical polarization, which allows it to be fully reflected by the PBS to the SLM. The reflected laser then enters the intensity modulation system, which consists of a QWP with its fast axis oriented at 45° relative to the horizontal direction, and the SLM, in which the liquid-crystal orientation is aligned horizontally.

As the vertically polarized laser passes through the QWP, a $\lambda/4$ phase difference is introduced between the fast axis and the slow axis, converting the laser into a circularly polarized beam. The Jones matrix for the QWP whose fast axis is positioned at 45° is

$$M_{\mathrm{QWP45}} = \begin{pmatrix} \cos 45^\circ & -\sin 45^\circ \\ \sin 45^\circ & \cos 45^\circ \end{pmatrix} \begin{pmatrix} 1 & 0 \\ 0 & \mathrm{j} \end{pmatrix} \begin{pmatrix} \cos 45^\circ & \sin 45^\circ \\ -\sin 45^\circ & \cos 45^\circ \end{pmatrix} = \frac{1}{2} \begin{pmatrix} 1+\mathrm{j} & 1-\mathrm{j} \\ 1-\mathrm{j} & 1+\mathrm{j} \end{pmatrix} \tag{1}$$

The horizontal component of the laser is then modulated by the SLM according to a projected phase pattern, with each SLM pixel assigned a specific phase delay δ, whereas the vertically polarized component remains unmodulated. The Jones matrix for the SLM is

$$M_{\mathrm{SLM}} = \begin{pmatrix} \mathrm{e}^{\frac{\mathrm{j}\delta}{2}} & 0 \\ 0 & \mathrm{e}^{-\frac{\mathrm{j}\delta}{2}} \end{pmatrix} \tag{2}$$

The modulated laser is reflected from the SLM and subsequently passes through the same QWP again. However, now the fast axis of the QWP becomes 135° owing to the opposite incident direction:

$$M_{\mathrm{QWP135}} = \begin{pmatrix} \cos 135^\circ & -\sin 135^\circ \\ \sin 135^\circ & \cos 135^\circ \end{pmatrix} \begin{pmatrix} 1 & 0 \\ 0 & \mathrm{j} \end{pmatrix} \begin{pmatrix} \cos 135^\circ & \sin 135^\circ \\ -\sin 135^\circ & \cos 135^\circ \end{pmatrix} = \frac{1}{2} \begin{pmatrix} 1+\mathrm{j} & \mathrm{j}-1 \\ \mathrm{j}-1 & 1+\mathrm{j} \end{pmatrix} \tag{3}$$

This entire phase-modulation process can be described using the Jones matrix as follows:

$$M = M_{\mathrm{QWP135}} M_{\mathrm{SLM}} M_{\mathrm{QWP45}} = \mathrm{j}\begin{pmatrix} \cos\left(\frac{\delta}{2}\right) & \sin\left(\frac{\delta}{2}\right) \\ -\sin\left(\frac{\delta}{2}\right) & \cos\left(\frac{\delta}{2}\right) \end{pmatrix} \tag{4}$$

After passing through the PBS, the output field is given by

$$\begin{aligned} f_{\mathrm{out}} &= M_{\mathrm{PBS}} M f_{\mathrm{in}} \\ &= \begin{pmatrix} 1 & 0 \\ 0 & 0 \end{pmatrix} \mathrm{j} \begin{pmatrix} \cos\left(\frac{\delta}{2}\right) & \sin\left(\frac{\delta}{2}\right) \\ -\sin\left(\frac{\delta}{2}\right) & \cos\left(\frac{\delta}{2}\right) \end{pmatrix} \mathrm{e}^{\mathrm{j}(\varphi_0)} \begin{pmatrix} 0 \\ 1 \end{pmatrix} \\ &= \mathrm{j}\mathrm{e}^{\mathrm{j}(\varphi_0)} \begin{pmatrix} \sin\left(\frac{\delta}{2}\right) \\ 0 \end{pmatrix} \end{aligned} \tag{5}$$

in which f_{in} is a vertically polarized beam with an initial phase of φ_0. As a result, the intensity at each pixel is modulated to

$$I_{\mathrm{out}} = I_{\mathrm{in}} \sin^2\left(\frac{\delta}{2}\right) \tag{6}$$

The curve (interpolated from the measured result) on the right side of Extended Data Fig. 3 is an example of how the intensity of a selected metalens focal spot can be modulated by varying the SLM pixel values (the SLM pixel value is linearly correlated to the applied phase delay δ). By applying different values to different SLM pixels, the laser can be effectively turned 'on' and 'off' and patterned in greyscale.

Uniformity correction for the focal spot array

First, we measure and correct the laser intensity distribution by visualizing the focal spot array using the microscope monitoring system shown in Extended Data Fig. 2. By sweeping the SLM phase values, we acquire a series of intensity measurements for the focal spot array. This dataset is then interpolated to establish the relationship between intensity and SLM phase value for each focal spot. The interpolation results are used to back-calculate the SLM phase pattern that generates a uniform focal spot array.

However, TPL is a highly sensitive nonlinear process. Owing to the mismatch in NA between the microscope system and the metalens, the intensity measurements are not accurate enough to perform high-quality parallel TPL. To address this, we further print a series of block patterns by finely adjusting the SLM phase values around the SLM phase pattern obtained from the previous step. After printing, we count the number of the printed blocks, using that as the direct evidence to determine the precise SLM phase values that ensures the intensities of the focal spots are uniform, as depicted in Supplementary Fig. 6. It is worth noting that such patterns can be designed in any form, such as lines, blocks, bars and so on.

The precision of this method is contingent on the tuning accuracy of the SLM values. Our SLM pixels have a bit depth of 8, with values ranging from 0 to 127 corresponding to 0 to π for optical phase. When using the 200-μm metalens array, each metalens is mapped to a 16 × 16 grid of SLM pixels, resulting in an effective tuning precision of 1/32,768. When using the 100-μm metalens array, each metalens is mapped to a 3 × 3 grid of SLM pixels, resulting in an effective tuning precision of 1/2,304.

Throughput scaling of AML

The effectiveness of AML depends on the information compressibility of the targeted 3D geometry. For a fully periodic structure with periodicity equal to the metalens pitch or the pitch divided by an integer, metalens TPL can be performed in which all focal spots are always on during path scanning, maximizing printing throughput. However, when printing non-periodic structures, only a fraction of focal spots is turned on at any point during path scanning, reducing the effective printing throughput. To quantify the effective throughput for a given structure, we define the compression factor to be $\eta_c = \frac{\text{average density}}{\text{overlaid density}}$ and the effective printing rate to be $\eta_c \times$ maximum voxel rate (Extended Data Fig. 7a). In Supplementary Fig. 11, we evaluate and compare the compression factors of various representative structures, including the periodic and semiperiodic structures, structures that have mismatched periodicity with the metalens array, coarse shapes and stochastic structures. As the number of metalenses increases and as the targeted structure becomes less periodic, the overlaid structure merges into a fully dense block with the size of a metalens, and the compression factor converges to the relative density of the targeted geometry. For example, for the Voronoi lattice shown in Fig. 3g, the compression factor is the same as its relative density of 0.252, meaning that even though there is no periodicity in this structure, AML can still print it at 25% of the maximum throughput. We visualize the scaling of TPL throughput using AML for printing structures with different degrees of structural compressibility in Extended Data Fig. 7b.

Fabrication and tensile testing for mechanical metamaterials

The samples are designed with dimensions 10.0 × 5.0 × 0.6 mm^3 to fit the testing set-up. The size of each unit cell of the lattices is 50 μm and the beam diameters are adjusted to achieve a relative density of 4% across all topologies (d = 3 μm for the octet lattice, d = 4 μm for the Kelvin lattice and d = 4.2 μm for the chainmail lattice). The chainmail lattices consist of columns of stacked truncated tetrahedron cages (unit cells) in the z direction (0.6 mm), which are interlocked with their neighbours in the x direction (10.0 mm) and the y direction (5.0 mm). Within each column in z, the neighbouring unit cells are flipping in the z direction and form mirrored images with one another. In this way, the truncated tetrahedron cages share one beam with their upper and lower neighbours, enabling them to be stacked rigidly in the z direction while being interlocked like a chainmail in the x and y directions. Uniaxial tensile loading is along the x direction. A notch opening, measuring 1.6 mm in length and 50 μm in width (equivalent to the width of one unit cell), is designed at the centre of the testing structure to guide crack growth. To create the notch, the SLM pixel values at the corresponding area are actively tuned (by turning the focal spot 'on' and 'off') during the scanning of the toolpath.

The testing samples are fabricated on silica substrates. To create the dogbone testing geometry, the samples are immersed in a custom ultraviolet (UV) resin composed of 69 wt% BPAGDA, 30 wt% PEGDA (M_n 250) and 1 wt% TPO-L immediately after fabrication. Each sample is patterned with a pair of gripping ends using a UV projector (Vistech), forming the dogbone structure. After that, the entire sample is sequentially developed in PGMEA, IPA and NOVEC 7100 to remove excessive resin and is then detached from the substrate using a razor blade. Before testing, the samples are post-cured in a UV box (Form Cure, Formlabs) for 1 h at room temperature.

Testing is conducted using a displacement-controlled device (Kammrath & Weiss Tensile & Compression Module), equipped with tensile grips (UL5) and a 10-N load cell. During the tests, the samples are displaced at a rate of 2 μm s^{-1} until full fracture. The experiments are performed under an optical microscope to capture real-time images.

Simulation of mechanical metamaterials

A hybrid FEM method is developed to conduct nonlinear static structural simulations for the octet and Kelvin lattices with Ansys R23.2. The lattices near the crack tip are modelled with beam elements and bilinear elastic–plastic material. The rest of the sample is modelled with hexagonal elements and orthotropic material model. The two sample areas are coupled together in the hybrid model. The overall

dimensions of the model are $2.5 \times 10.0 \times 0.1\ mm^3$. Symmetry boundary condition is used, so only half of the sample is simulated (as shown in Extended Data Fig. 9). The overall size of the beam elements region is $0.45 \times 0.55 \times 0.10\ mm^3$. The orthotropic properties are obtained by homogenizing the topology using nTopology. Beam and hexagonal elements are quadratic, element size of the beam elements is 5 µm and the size of the hexagonal elements is 50 µm. Mechanical parameters used for the beam element are as follows: Young's modulus 2.5 GPa, yield stress 100 MPa, plastic tangential modulus 0.625 GPa, fracture stress 220 MPa (0.19 plastic strain) and density 1,000 kg m^{-3}. We simulate the octet and Kelvin samples under tension until just before fracture, when one meshed element in the discrete region reaches the fracture strength, and we visualize the approximate size of the plastic zone by colouring in red the elements with a von Mises stress above the yield stress of 100 MPa (Fig. 4f,i). Because the Kelvin lattice presents most of the plastic deformation in the node right at the union of different beams, the elemental difference equivalent stress is shown Fig. 4i. In this case, the elemental difference equivalent stress highlights the element that has a node that undergoes plasticity.

LS-DEM[53] is used to qualitatively simulate the breakage process of the chainmail lattices in the tension experiment. To enhance computational efficiency, we construct cell pillars consisting of only four vertically stacked polyhedron cages in Cinema 4D. The four unit cells are merged into one entity to ensure smooth and consistent surface meshing. The meshed entity is then output as an STL file with 37,764 faces to ensure sufficient accuracy. The STL file is then converted to a grid-point representation following the level set method, whereas each entity is referred to as a particle. A sample measuring 73 × 36 particles is then assembled, with 12 particles along the middle vertical line removed to create a pre-existing crack. Particles are initialized without contact, with the two short edges fixed. Local and global damping is added to aid stability. Gravity is first applied until equilibrium is reached, after which the two short edges are pulled apart at a constant strain of 0.024% per interval. To determine the breakage criteria, we first calculate the average particle stress, followed by the von Mises stress. If the calculated stress exceeded a predefined threshold, the particle is deemed 'broken' and subsequently removed. Stress concentrations are observed at the crack tips as well as along the horizontal line of connected particles in the loading direction, perpendicular to the notch. Owing to the high stress experienced by particles at the crack tips, stress propagates along the loading direction through force chains, transferring the load to connected particles.

Fabrication of THz metamaterials

We use metalens TPL to fabricate large-area THz metamaterials. Electromagnetic metamaterials are of particular interest for the THz frequency range (0.1–10.0 THz) because there is a lack of natural materials suitable for manufacturing functional THz optical components such as beam splitters, waveplates and polarizers[54–56]. TPL is particularly well suited for fabricating THz metamaterials owing to its ability to produce subwavelength-scale structures (<30–3,000 µm) with optical-grade smoothness and to enable truly 3D metamaterial architectures for advanced wave control. However, the fabrication of THz metamaterials with conventional TPL has been limited to small device sizes, which have hindered their practical applications. We present the fabrication of centimetre-sized THz metamaterials consisting of thousands of subwavelength-scale helical meta-atoms that support broadband circular polarization modulation. The helical unit has a major diameter of 120 µm, a wire diameter of 32 µm and an axial pitch of 200 µm (Supplementary Fig. 12a). After printing, the helical structure is coated with 1 µm Au, embedded in polydimethylsiloxane (PDMS) and detached from the substrate as a flexible device, as illustrated in Supplementary Fig. 12b.

Extended Data Fig. 10a shows the well-defined helix array structures ($10.0 \times 10.0 \times 1.2\ mm^3$) before PDMS embedding. The THz metamaterial demonstrates clean band-pass polarization filtering over a wide working spectrum (0.2–1.2 THz) and it transmits left-hand circular polarized light from 0.20 to 0.65 THz and right-hand circular polarized light from 0.65 to 1.20 THz, which is in good agreement with the simulation (Extended Data Fig. 10c and Supplementary Fig. 12c). By spatially patterning helical structures of different handedness, we can transmit images with a circular polarization basis. We encode a letter 'S' into a THz metamaterial device as a demonstration (Extended Data Fig. 10d), which we can visualize using a custom THz imaging system at around 1 THz (Extended Data Fig. 10f). We anticipate that these large-scale, flexible THz metamaterial devices have potential applications in the domains of security and anti-counterfeiting, information processing, biosensing and flexible electronics.

Data availability

All data are available in the main text, Methods or in the Supplementary Information. Other information related to this study is available from the corresponding author on request.

51. Hugonin, J. P. & Lalanne, P. RETICOLO software for grating analysis. Preprint at https://arxiv.org/abs/2101.00901 (2025).
52. Holzwarth, C., Barwicz, T. & Smith, H. I. Optimization of hydrogen silsesquioxane for photonic applications. *J. Vac. Sci. Technol. B* **25**, 2658–2661 (2007).
53. Kawamoto, R., Andò, E., Viggiani, G. & Andrade, J. E. Level set discrete element method for three-dimensional computations with triaxial case study. *J. Mech. Phys. Solids* **91**, 1–13 (2016).
54. Choi, W. J. et al. Terahertz circular dichroism spectroscopy of biomaterials enabled by kirigami polarization modulators. *Nat. Mater.* **18**, 820–826 (2019).
55. Choi, W. J., Lee, S. H., Cha, M. & Kotov, N. A. Chiral kirigami for bend-tolerant reconfigurable hologram with continuously variable chirality measures. *Adv. Mater.* **36**, e2401131 (2024).
56. Choi, W. et al. Helical photonic metamaterials for encrypted chiral holograms. *Adv. Sci.* **12**, e07931 (2025).

Acknowledgements X.X. and J.A.F. acknowledge financial support from Lawrence Livermore National Laboratory's Lab Directed Research and Development Program (LDRD: 22-ERD-004) for funding most of the project and making the research possible. S.G. acknowledges financial support from Lawrence Livermore National Laboratory's Lab Directed Research and Development Program (LDRD: 25-LW-103) for supporting the final stage of the project. Work at LLNL was performed under the auspices of the U.S. Department of Energy by Lawrence Livermore National Laboratory under contract DE-AC52-07NA27344. J.A.F. acknowledges further support from the Packard Foundation under grant number 2016-65132 and the National Science Foundation under award number 2103721. W.Z. and C.D. acknowledge support from the Army Research Office (MURI ARO W911NF-22-2-0109).

Author contributions S.G. and X.X. designed and built the printing system and performed the printing and the characterization experiments. C.M. designed, modelled and fabricated the metalens, with help from T.M., A.A. and Y.Z. A.G.I. generated the printing toolpaths, performed mechanical testing and performed simulation for the octet and Kelvin lattices, with help from X.X. and S.G. D.T.-P. and S.S. developed the laser patterning function with help from T.U.T. and performed printing experiments. M.M.-Y. developed the photoresin with help from S.H. S.S., S.G. and X.X. developed the algorithm for printing arbitrary structures. W.C. designed and characterized the THz metamaterial. W.Z., C.D. and X.X. designed the chainmail lattice. W.Z., H.Y. and Z.Z. performed the simulation for the chainmail lattice. S.H. and C.M. modelled the proximity effect. X.X., J.A.F. and T.U.T. conceived the study. S.G. and X.X. prepared the manuscript, with revisions from all authors.

Competing interests A US patent and three US patent applications related to this work have been filed, with S.G., S.S., A.G.I., D.T.-P., T.U.T. and X.X. as co-inventors. The authors declare no other competing interests.

Additional information

Supplementary information The online version contains supplementary material available at https://doi.org/10.1038/s41586-025-09842-x.

Correspondence and requests for materials should be addressed to Jonathan A. Fan or Xiaoxing Xia.

Peer review information *Nature* thanks Liang Pan, Wei Xiong and the other, anonymous, reviewer(s) for their contribution to the peer review of this work. Peer reviewer reports are available.

Reprints and permissions information is available at http://www.nature.com/reprints.

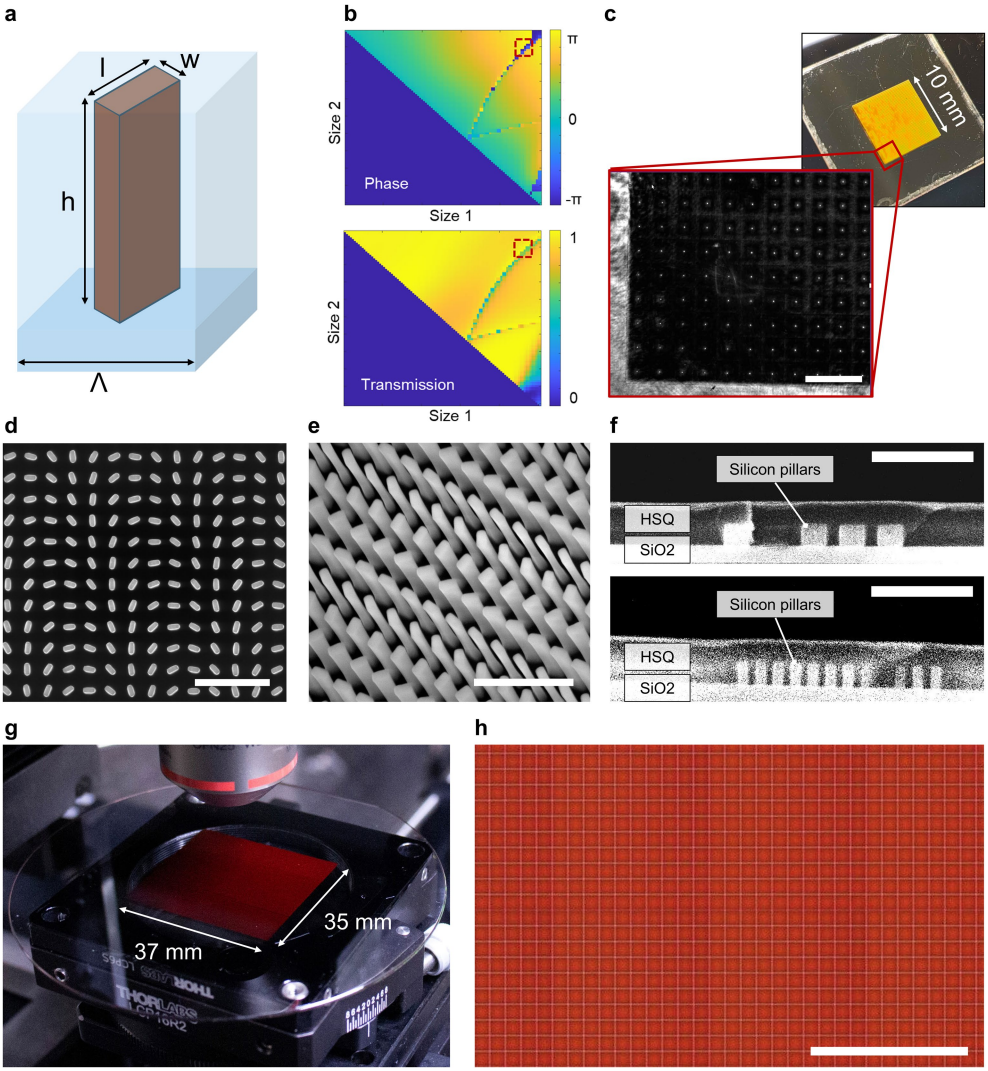

Extended Data Fig. 1 | Metalens design and fabrication. a, Unit cell of geometric-phase meta-atom. Λ: period, 300 nm; l: 190 nm; w: 111.0 nm; h: 785.0 nm. **b**, Sweeps of rectangle side lengths. Top, phase difference between x and y polarized responses. Bottom, transmission. The red boxes indicate optimal design with π phase difference and near-unity transmission. **c**, Photo of the 50 × 50, NA 1.0 metalens array (lens size: 200 µm, array size: 10 × 10 mm^2) and the focal spots of lenses (in air) under an optical microscope. Scale bar, 500 µm. **d**,**e**, SEM images of the top view and the tilted view of the nanopillars. Scale bars, 1 µm. **f**, Cross-section SEM view of a test wafer, in which the silicon nanostructures are embedded in HSQ. Two layers of HSQ were spun on, with rapid thermal annealing applied after each layer. Gaps between the nanopillars, which are smaller than 100 nm, are fully filled without trapped air. Scale bar, 1 µm. **g**, Photo of the 370 × 350, NA 0.8 metalens array (lens size: 100 µm, array size: 37 × 35 mm^2). **h**, Zoomed-in optical image of the metalenses. Scale bar, 1 mm.

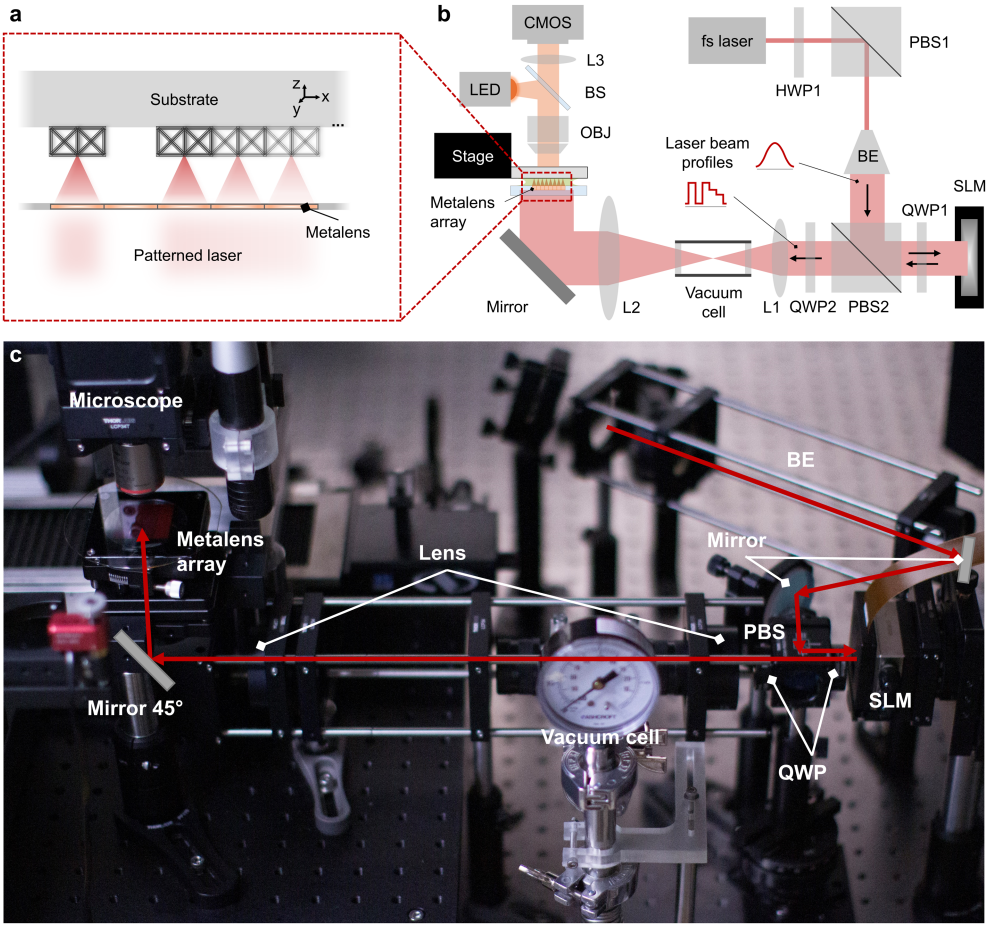

Extended Data Fig. 2 | Metalens-based TPL system. a,**b**, Schematic of the metalens-based TPL system and a zoomed-in view showing the printing of gradient structures with patterned laser beam. HWP1, HWP2: half-wave plates; PBS1, PBS2: polarization beam splitters; QWP1, QWP2: quarter-wave plates; L1, L2, L3: lenses; BE: beam expander; OBJ: objective lens; BS: beam splitter. **c**, Photo of the optical set-up.

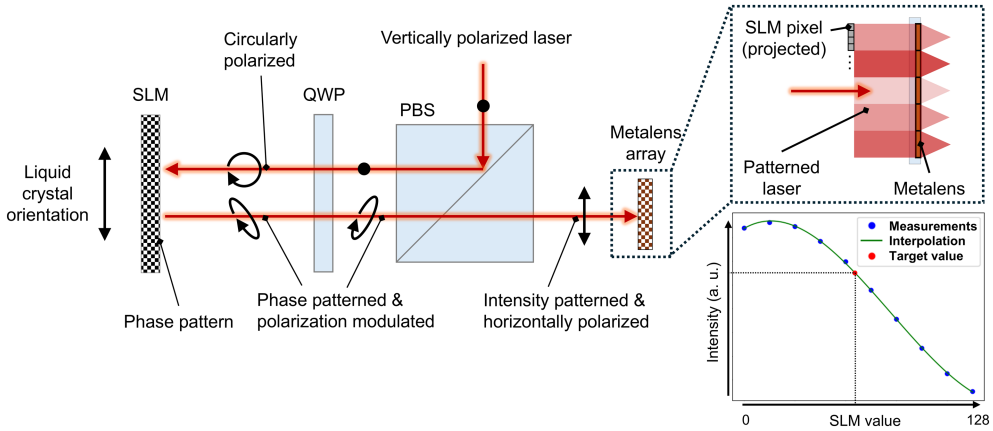

Extended Data Fig. 3 | Principle of phase-to-amplitude modulation using a liquid-crystal SLM. A vertically polarized laser is reflected by a polarization beam splitter (PBS) and modulated by a quarter-wave plate (QWP). Then, the laser is incident onto the liquid-crystal SLM, modulated pixel by pixel within the liquid-crystal orientation plane. After that, the laser passes through the QWP and the PBS to become an intensity-modulated laser beam and is finally projected onto the metalens array. The 4*f* system between the phase-to amplitude modulation subsystem and the metalens is omitted here for simple illustration purposes. An example of modulating the laser intensity with SLM pixel value is shown in the chart in the bottom-right corner. a.u., arbitrary units.

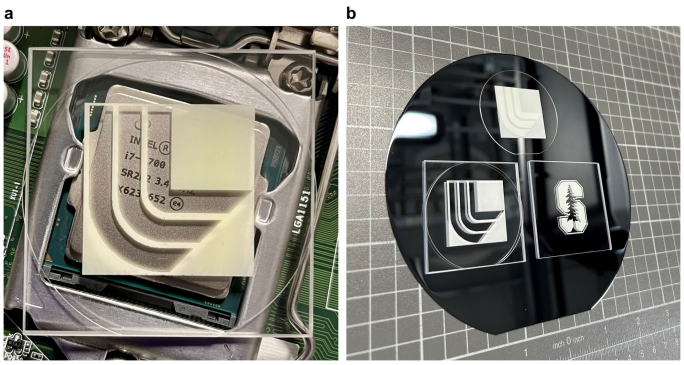

Extended Data Fig. 4 | Gallery of 3-cm 3D architectures with sub-micrometre resolution. a, A LLNL logo with some focal spots turned off. A central processing unit chip is placed underneath for size reference. **b**, LLNL logos and a Stanford logo. A 6-inch wafer is placed underneath for size reference.

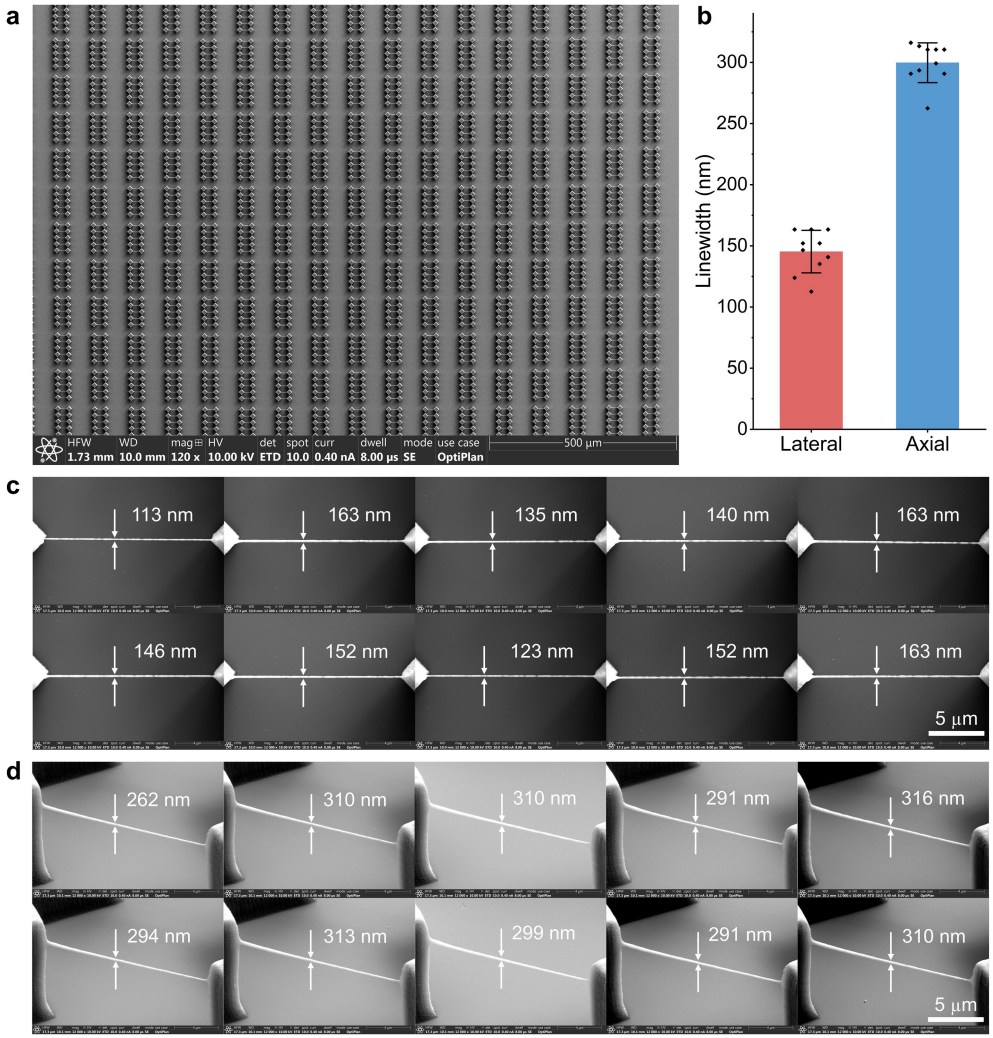

Extended Data Fig. 5 | Measurement of subdiffraction linewidths. a, SEM image of a large array of suspended nanowires printed by a uniformity-corrected system (metalens NA: 1.0). **b**, A survey of lateral and axial linewidths by randomly selecting lines printed by different metalenses (standard deviation = 16.5 nm (lateral) and 15.4 nm (axial), $n = 10$). **c**, Lateral measurements for randomly selected nanowires. **d**, Axial measurements for randomly selected nanowires.

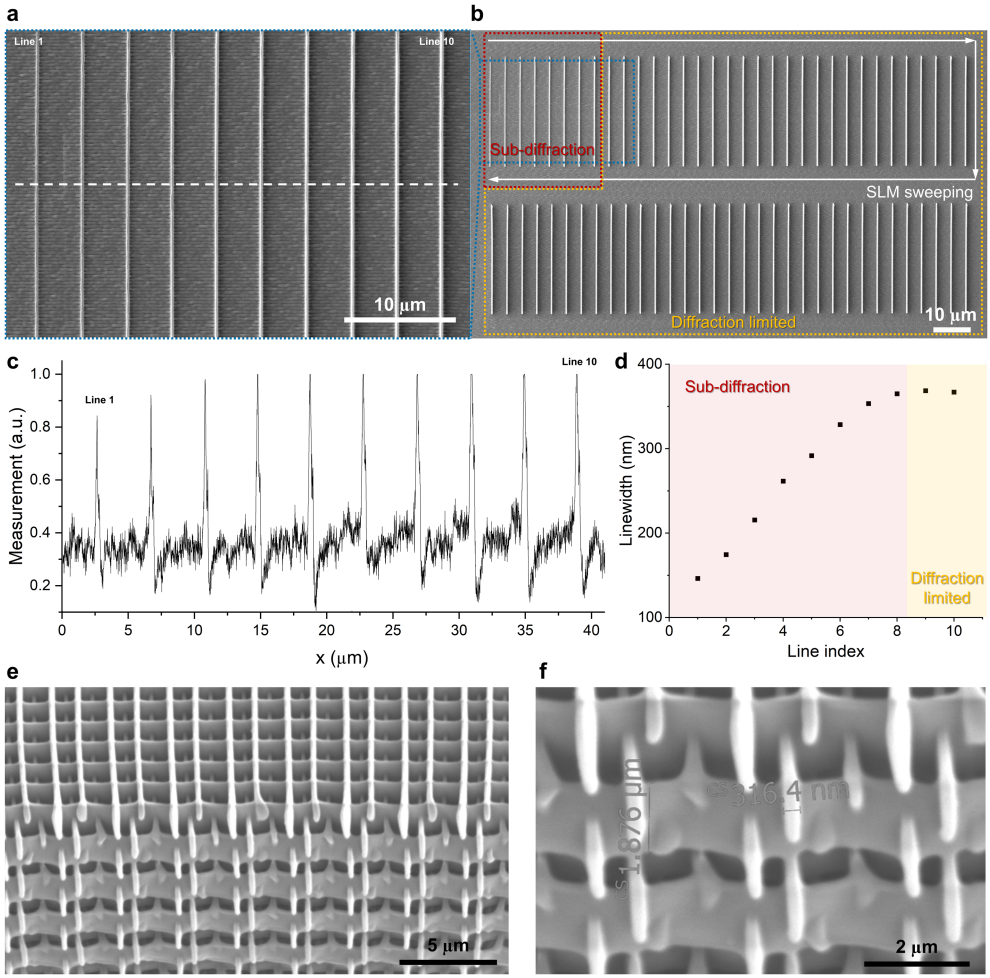

Extended Data Fig. 6 | Greyscale printing by means of SLM tuning. a,**b**, SEM images of a line array printed by sweeping the SLM phase value (metalens NA: 1.0). Specific SLM values are not listed owing to different settings for each metalens. **c**,**d**, Measurements of linewidths in **a** showing tunable voxel size at the subdiffraction regime and stable voxel size at the diffraction-limited regime. **e**,**f**, SEM images of 3D subdiffraction features. The measured lateral and axial linewidth are 316.4 nm and 1.876 μm, respectively.

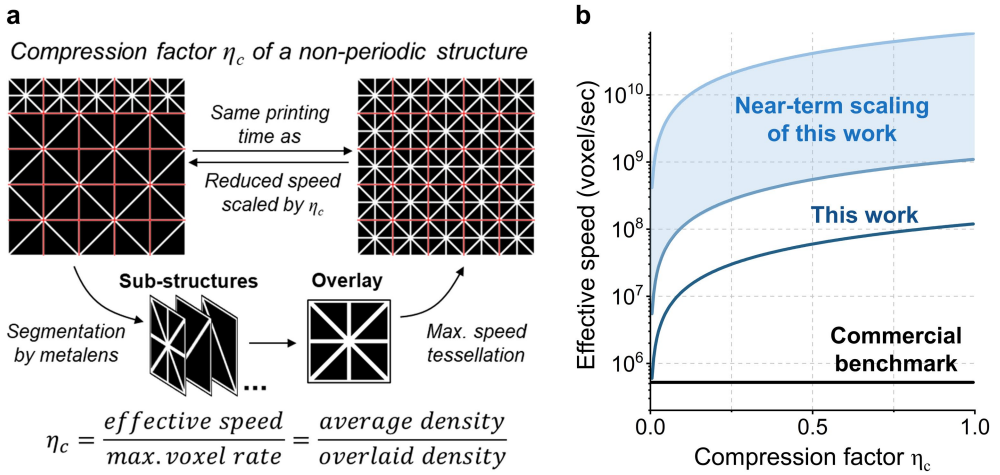

Extended Data Fig. 7 | Structural compression and throughput scaling. **a**, Definition of the compression factor of a structure. As an example, the structure is divided into 5 × 5 substructures. Then, all of the substructures are overlaid to obtain the compressed structure. The stage scans over the entire compressed structure with active focal spot modulation to print the desired structure. It can be derived that the compression factor is determined by the average density and the overlaid density of the structure. **b**, Chart showing the effective fabrication speed with varying compression factors. The near-term scaling of this work is discussed in section 'Discussion on the current limit and near-term scaling of the fabrication throughput' in the Supplementary Information.

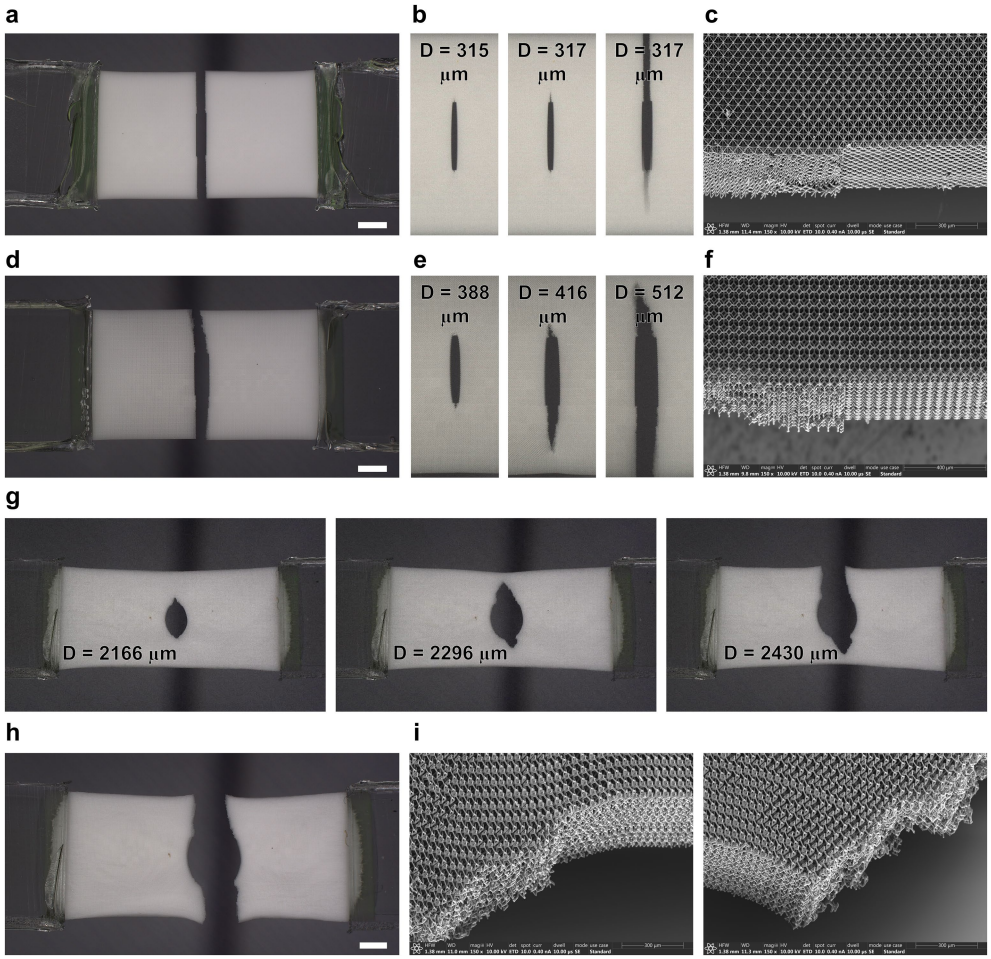

Extended Data Fig. 8 | Images for the tensile experiments of an octet, a Kelvin and a chainmail lattice. a, Fractured octet lattice. Scale bar, 1 mm. **b**, Zoomed-in crack frames for the octet lattice. *D*: displacement. **c**, SEM image of the fractured octet near the notch. **d**, Fractured Kelvin lattice. Scale bar, 1 mm. **e**, Zoomed-in crack frames for the Kelvin lattice. **f**, SEM image of the fractured Kelvin lattice near the notch. **g**, Crack frames for the chainmail lattice. **h**, Fractured chainmail lattice. Scale bar, 1 mm. **i**, SEM images of the fractured chainmail lattice near the notch.

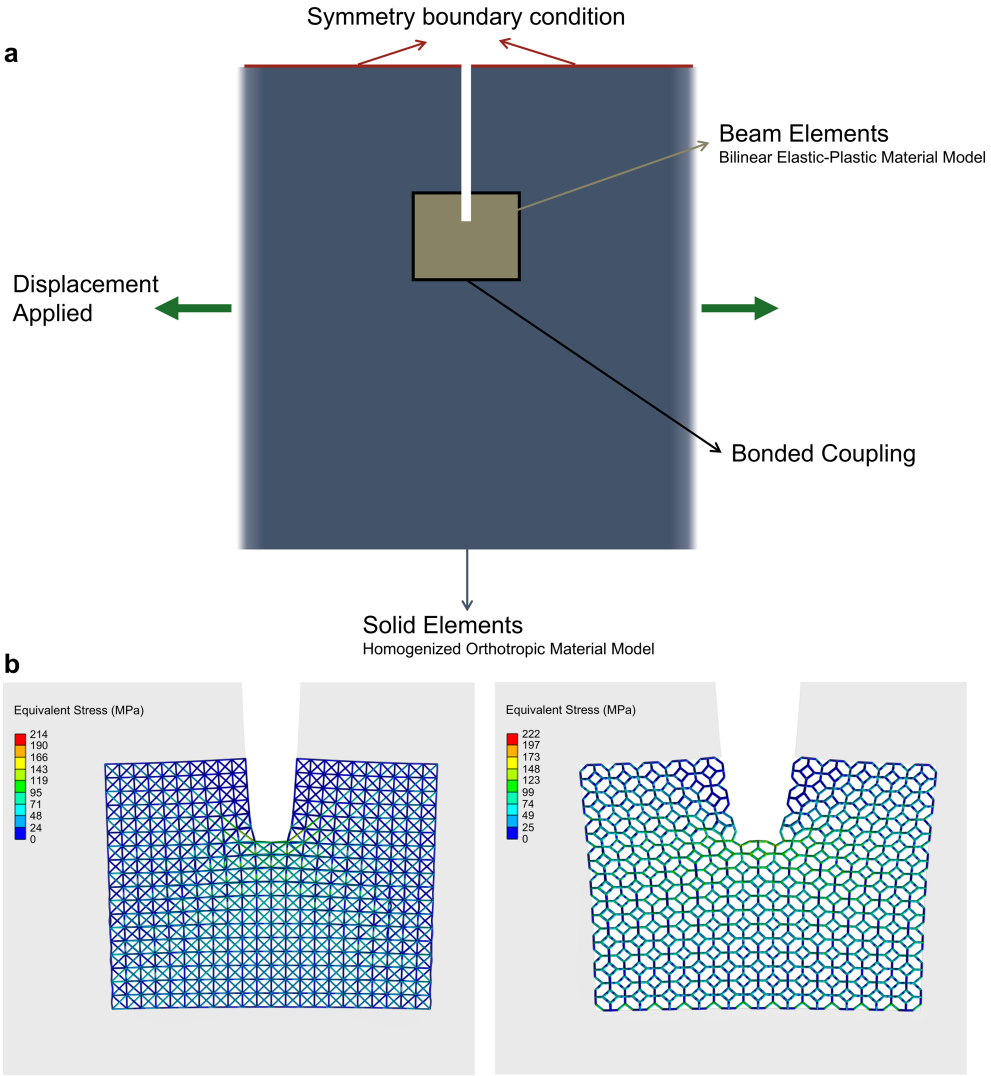

Extended Data Fig. 9 | Hybrid FEM model for simulating the large-scale octet and Kelvin lattices. a, Schematic of the hybrid model, in which the lattices near the crack tip are modelled as beam elements and the rest of the sample is modelled as solid elements. **b**, Simulated stress distribution before crack propagation.

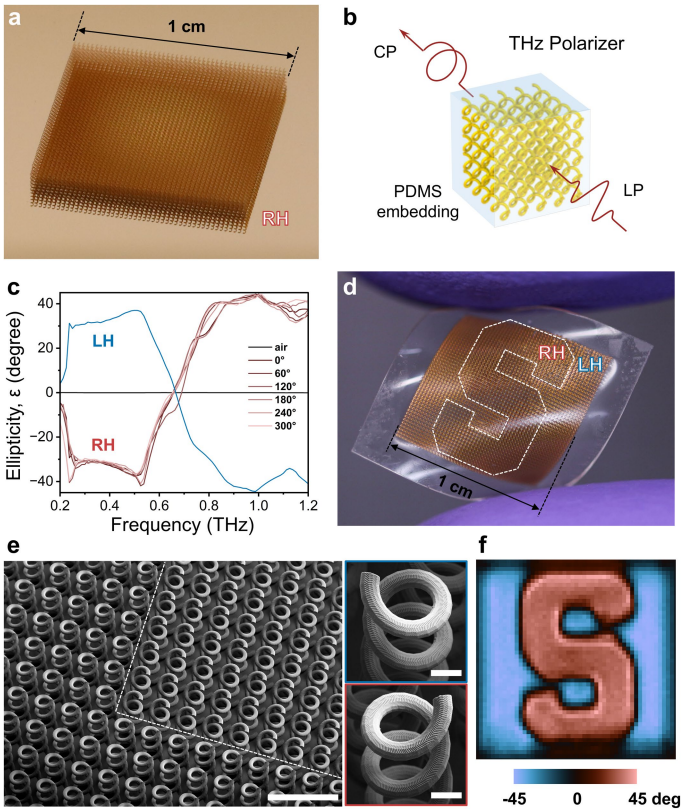

Extended Data Fig. 10 | Fabrication of large-scale THz metamaterials. **a**, A right-handed (RH) 1-cm^2 helical THz metamaterial fabricated using metalens-based TPL and coated with gold before embedding in PDMS. **b**, Principle of using such helical THz metamaterials as transmission polarizers. The gold-coated structure is embedded in PDMS and detached from the substrate. **c**, Measured ellipticity of the left-handed (LH) and RH THz polarizers from 0.2 THz to 1.2 THz. The RH polarizer is measured with different incident angles to demonstrate robust chirality. **d**, A 1-cm^2 THz metamaterial patterned with both RH and LH helices, embedded in PDMS and detached from the rigid substrate for flexible applications. **e**, SEM images of the fabricated helices with both LH and RH regions. Scale bars, 500 μm (zoomed-out view); 50 μm (zoomed-in view). **f**, Measured ellipticity map of the THz metamaterial in **d** at 1.012 THz. The unit-cell design and dimensions are given in Supplementary Fig. 12a.